ARTICLE OPEN

Check for updates

Study on corrosion, hydrogen permeation, and stress corrosion cracking behaviours of AISI 4135 steel in the tidal zone

Yong Xu[1,2,3,4], Yanliang Huang [1,2,4✉], Fanfan Cai[1,2,3,4], Dongzhu Lu[1,2,4✉], Zhengquan Wang[1,2,3,4] and Xiutong Wang[1,2,4]

High-strength steels are widely used in marine engineering; however, they suffer from the risks of corrosion, hydrogen permeation, and stress corrosion cracking (SCC) in wet–dry cyclic marine environments. In this study, the corrosion, hydrogen permeation, and SCC behaviours of AISI 4135 steel in the tidal zone were investigated using electrochemical corrosion, electrochemical hydrogen permeation, and slow strain rate tests, respectively, via field exposure. The results showed that the AISI 4135 steel sample placed at the high tide level had high SCC susceptibility because of severe pitting corrosion and hydrogen permeation, whereas the steel samples placed at the middle and low tide levels had low SCC susceptibilities. The dry/wet time ratio was crucial in determining the SCC behaviour and mechanism of the steel in the tidal zone. With increasing time ratio, the SCC mechanism changed from micro-void coalescence control to localised anodic dissolution and hydrogen embrittlement in tandem.

INTRODUCTION

With the extensive exploitation of ocean resources worldwide, high-strength steels are being widely used in marine engineering applications, such as offshore oil and gas transport pipelines and wind power facilities, owing to their good mechanical properties. However, the safety and reliability of high-strength steel structures in harsh marine environments are of significant concern. On the one hand, high-strength steels are vulnerable to corrosion and hydrogen permeation caused by high-salt environments in the long term[1,2]; on the other hand, load bearing poses more serious challenges to high-strength steel structures[3]. Under the synergy between the aforementioned factors, high-strength steels are at a high risk of stress corrosion cracking (SCC) during service, and the risk increases with the material strength[4]. Over the past few decades, SCC has been recognised as one of the most important causes of structural accidents, significantly limiting the further application of high-strength steels in future ocean development.

High-strength steels are much prone to corrosion and SCC in wet–dry cyclic marine environments because of dry/wet surface alternation, salt deposition, and full aeration[5–7]. Hao et al.[8] found out that E690 steel has high SCC susceptibility in wet–dry cyclic marine environments, and the SCC mechanism is a combination of anodic dissolution (AD) and hydrogen embrittlement (HE). Gong et al.[9] showed that X100 steel covered with a rust layer has high SCC susceptibility under alternating dry/wet conditions and that the rust layer facilitates SCC in the presence of Cl^-. However, most studies on the SCC behaviour of steel in wet–dry cyclic marine environments have been conducted indoors; the differences between the simulated and actual marine environments due to factors such as sunshine, tidal shock, and biofouling may lead to discrepancies between results and misinterpretation of the SCC behaviour. For example, Zhou et al.[10] reported the non-existence of pits on the X80 steel surface after multiple simulated tidal cycles in seawater, whereas Yu et al.[11] reported that high-strength steel exhibits a temperature-dependent pitting behaviour in natural

wet–dry cyclic marine environments. Furthermore, crevice corrosion or localised corrosion of steel caused by macro-fouling species such as barnacles and oysters in field marine environments was also reported in many studies[12–14]. Therefore, the investigation of corrosion and SCC behaviours of high-strength steels in natural wet–dry cyclic marine environments, especially considering the promoting effect of pitting corrosion or local corrosion on SCC, is of practical significance[6,15].

Both AD and HE are involved in the SCC of steel in marine environments; however, the contribution of AD or HE to SCC initiation and propagation depends on the external environment[15,16]. Currently, the corrosion behaviour and hydrogen absorption of high-strength steels in simulated or natural marine environments have been widely studied for examining their effects on the mechanical properties of steel[1,17]. However, in situ monitoring of hydrogen permeation into steel is extremely difficult compared to the in situ corrosion monitoring of steel in natural marine environments. Our literature survey shows that the works reported to date involve only in situ monitoring studies of hydrogen permeation into steel in natural marine atmospheric environments[18]; for highly complex marine environments, hydrogen permeation tests have mostly been conducted indoors[19,20]. Nevertheless, considering the close relationship between the hydrogen permeation, corrosion, and HE, it is important to clarify the hydrogen permeation process and the amount of hydrogen permeated into steel under natural corrosion conditions in marine environments. Huang et al.[21] discovered that the amount of hydrogen permeated into steel is positively related to the corrosion loss of steel and that the hydrogen ions derived from the hydrolysis of corrosion products are one of the main sources of hydrogen. However, the cathodic hydrogen evolution reaction can further accelerate metal corrosion[22]. Zhang et al.[23] studied the effect of hydrogen partial pressure on the fracture toughness and fatigue life of a high-strength pipeline steel and reported that 3% hydrogen gas is sufficient to decrease the fatigue life of the steel by 67.7%. Therefore, two factors are important for studying the
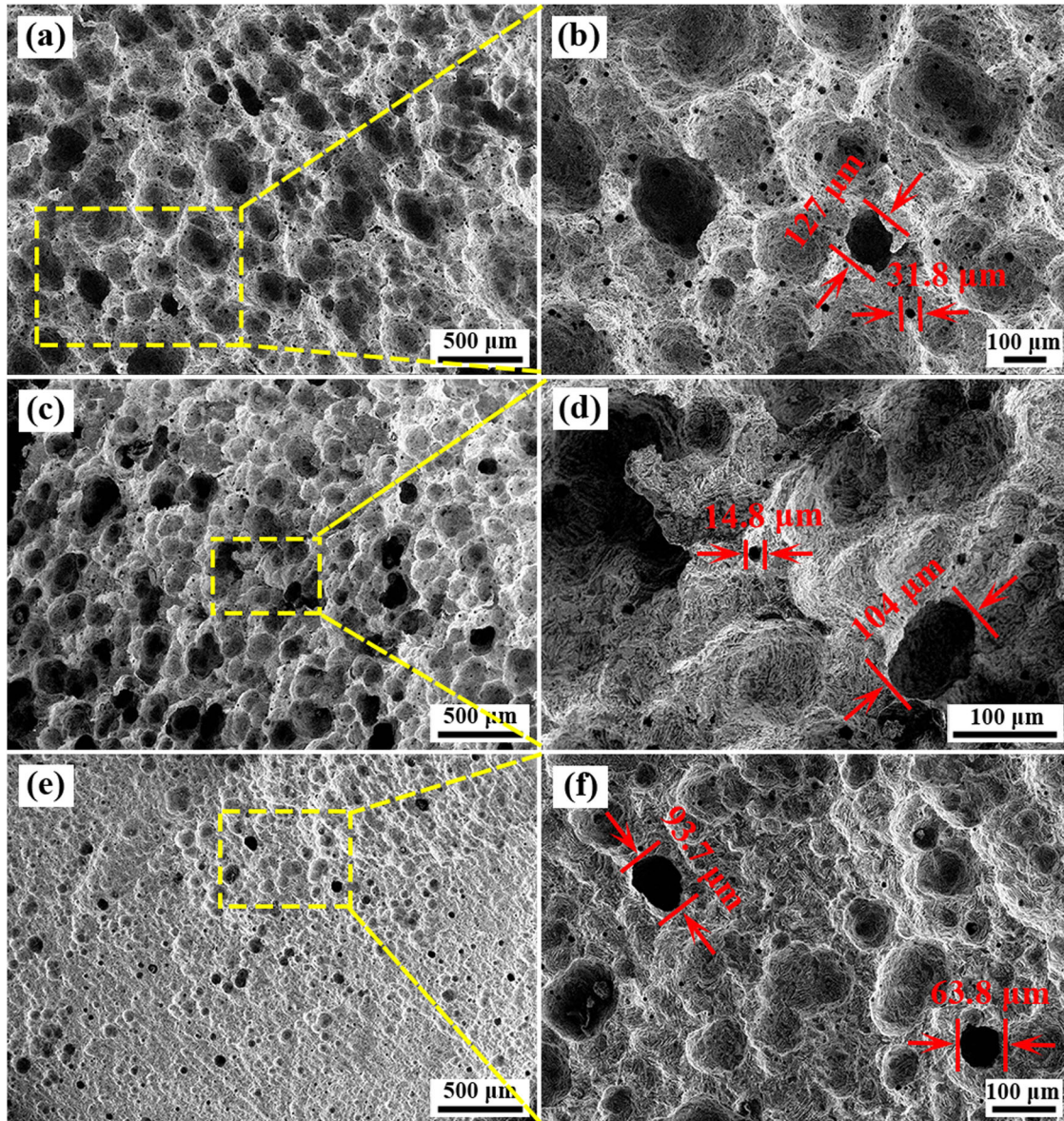
Fig. 1 SEM images of the coupons after exposure to the tidal zone. Corrosion morphologies of the matrix for the AISI 4135 steel coupons after exposure to the **a, b** HTL, **c, d** MTL and **e, f** LTL for 3 months.

SCC behaviour and mechanism of high-strength steel in wet–dry cyclic marine environments: consideration of a real marine environment as the research background and a simultaneous investigation of the possible influencing factors, especially corrosion and hydrogen permeation of steels.

In this study, field exposure tests of AISI 4135 steel were conducted in the tidal zone to investigate the corrosion, hydrogen permeation, and SCC behaviours of high-strength steels in wet–dry cyclic marine environments. Electrochemical impedance spectroscopy (EIS) and potentiodynamic polarisation curve tests were performed to examine the electrochemical corrosion behaviour of the steel during field exposure. The corrosion morphology and corrosion products of AISI 4135 steel after the field exposure tests were characterised by scanning electron microscopy (SEM), confocal laser scanning microscopy (CLSM), X-ray diffraction (XRD), energy dispersive spectroscopy (EDS) and Raman spectroscopy. An in situ hydrogen permeation monitoring system was developed based on electrochemical hydrogen permeation technology and used for continuously monitoring

the hydrogen permeation behaviour of the steel during the field exposure tests. The SCC behaviour of the steel after the field exposure was studied by slow strain rate test (SSRT) and SEM. The ultimate aim of this study is to provide a valuable reference for the safe application of high-strength steels in marine environments by analysing the corrosion, hydrogen permeation, and SCC behaviours and mechanisms of AISI 4135 steel in the tidal zone.

RESULTS

Surface corrosion morphology
Supplementary Fig. 1 shows the macroscopic morphologies of the corrosion coupons after exposure to the tidal zone for 3 months; all coupons were influenced by biofouling to different degrees. The surface morphology of the coupons was characterised by SEM after removing the corrosion products, and the results are shown in Fig. 1. All coupons in the tidal zone were characterised by pitting corrosion; the pits on the surface of the sample placed at
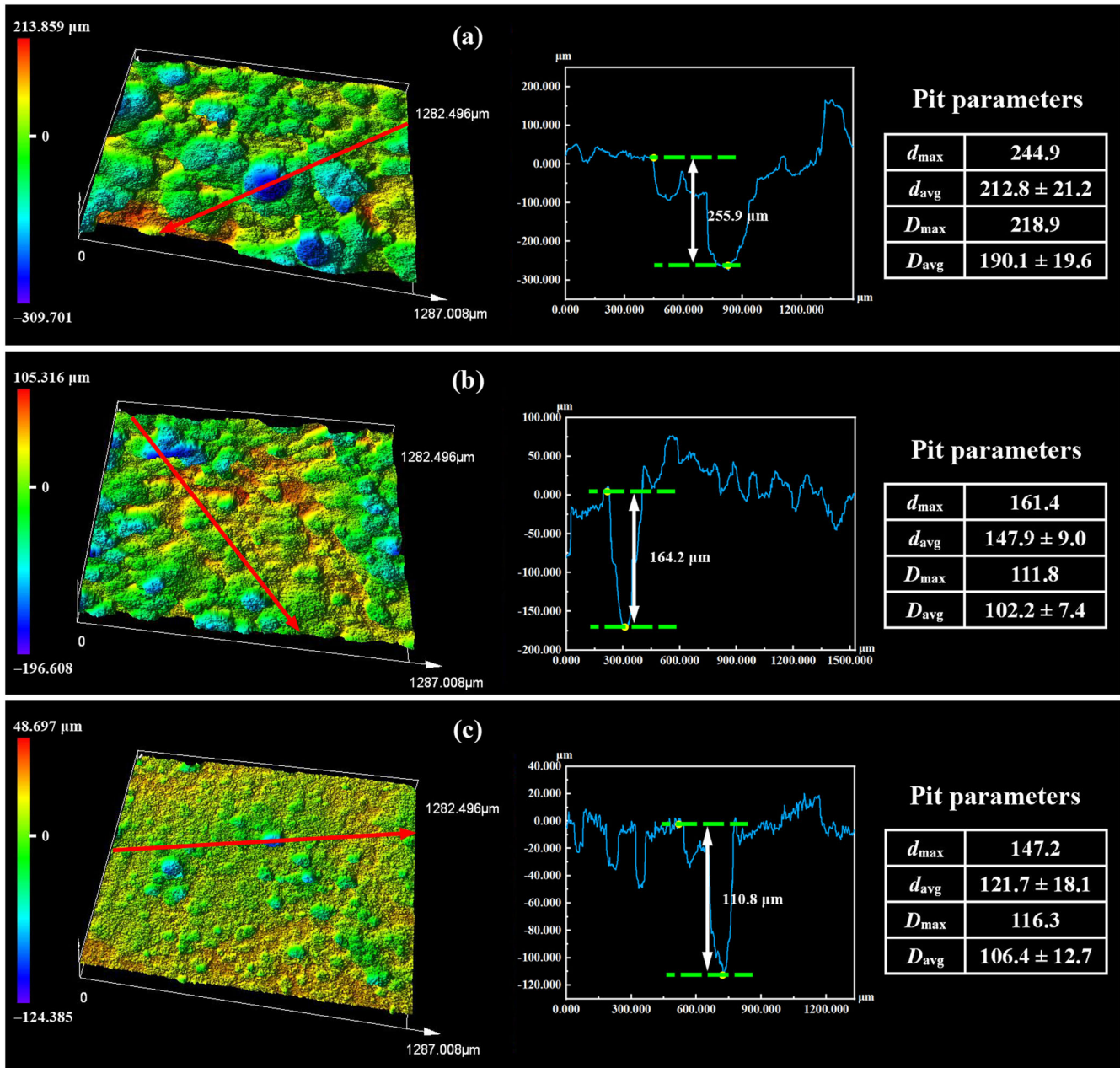
Fig. 2 CLSM images and corrosion pit parameters of the coupons after exposure to the tidal zone. CLSM images and corrosion pit parameters for the AISI 4135 steel coupons after exposure to the **a** HTL, **b** MTL and **c** LTL for 3 months.

the high tide level (HTL) had a significantly larger diameter than those of the samples placed at the middle tide level (MTL) and low tide level (LTL). Under stress, cracks largely tend to initiate and propagate at corrosion pits owing to the stress concentration[8,17]. Newman et al.[24] discovered that the geometry of the corrosion pit, especially the depth, significantly influences the crack initiation. Therefore, the 3D topography and pit parameters of the coupons were characterised by CLSM, and the results are shown in Fig. 2. The average pit diameters (D_{avg}) of the coupons placed at the HTL, MTL, and LTL were 190.1 ± 19.6, 102.2 ± 7.4, and 106.4 ± 12.7 μm, respectively. In addition, the average pit depths (d_{avg}) of the coupons placed at the HTL, MTL, and LTL were 212.8 ± 21.2, 147.9 ± 9.0, and 121.7 ± 18.1 μm, respectively. These results indicate that pitting corrosion is the main form of corrosion for AISI 4135 steel in the tidal zone; the higher the position of the

coupon in the tidal zone, the greater the depth and the larger the diameter of the corrosion pits.

Cross-sectional morphology and elemental distribution by SEM and EDS

Figure 3 shows the cross-sectional morphology and elemental distribution of the corrosion product layer (CPL) formed on the surface of the corrosion coupons after exposure to the tidal zone for 3 months. The CPL formed at the HTL was about 1.11 mm thick, whereas that formed at the MTL and LTL was 990 and 730 μm, respectively. The thickness of the CPL can partially elucidate the corrosion rate differences of the coupons. The cross-sectional morphologies revealed that the coupon placed at the HTL had a higher corrosion rate than the coupons placed at the MTL and LTL. All CPLs had a layered structure (Fig. 3), which could
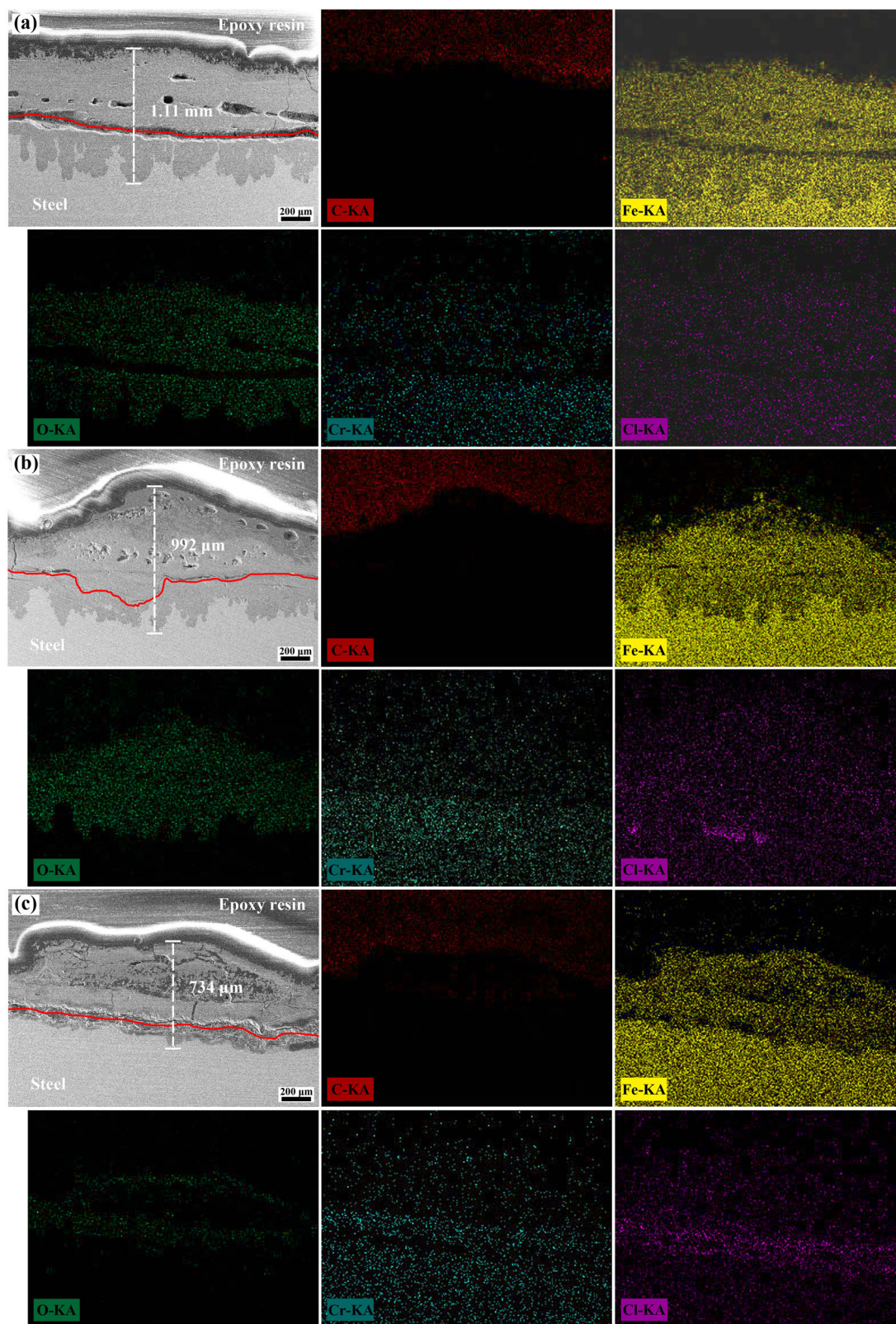
Fig. 3   SEM images and elemental distribution of the CPLs. SEM images and elemental distribution of the cross-section of the CPL formed on the surface of the AISI 4135 steel coupons after exposure to the **a** HTL, **b** MTL, and **c** LTL for 3 months.

be divided into inner and outer layers, and many holes and cracks were present in the CPLs. These CPLs with layered structures, holes and cracks mean that their inhibitory effect on the penetration of corrosive species, especially small-radius Cl⁻, is limited, as evidenced by the clear distribution of chlorine in the inner and outer layers (Fig. 3). In addition, the elemental distribution also shows that the corrosion products were rich in Cr and Fe. The high content of Cr in corrosion products implies
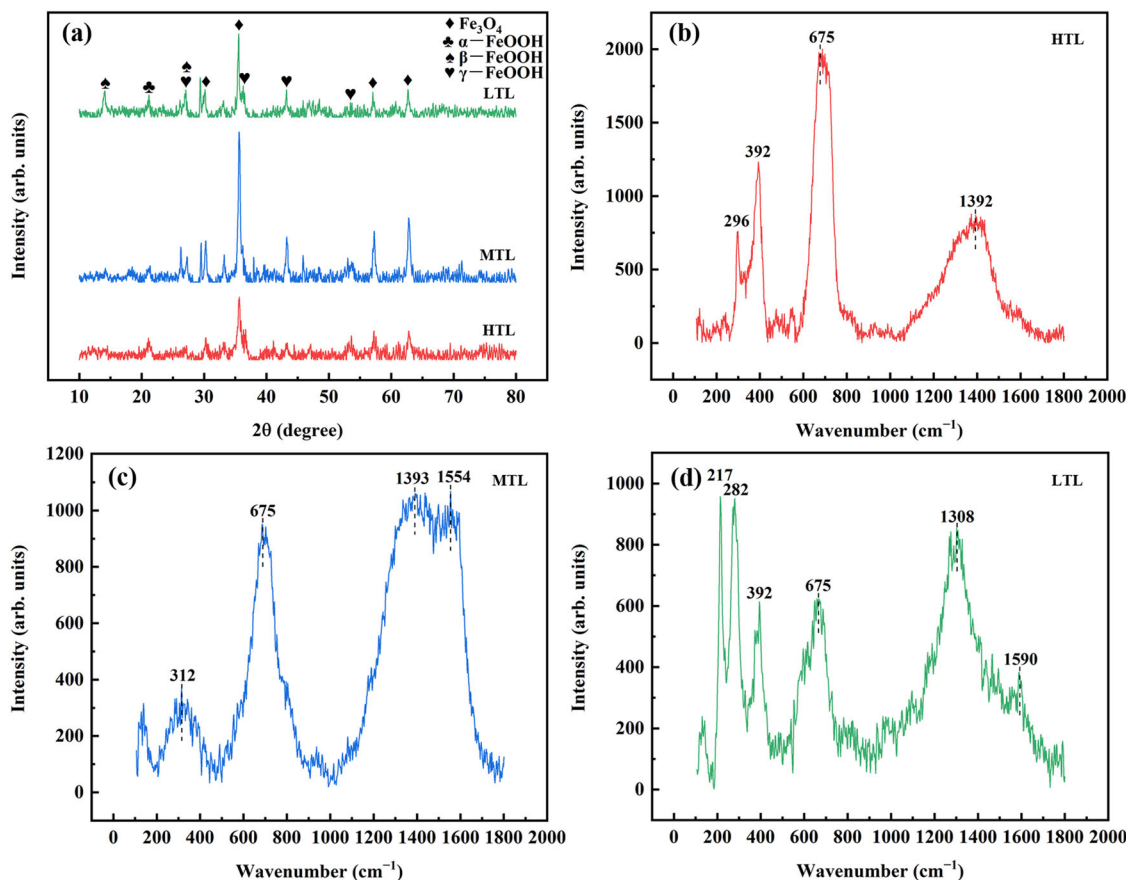
Fig. 4 Component analysis of the corrosion products formed on the surface of the AISI 4135 steel coupons after exposure to the tidal zone for 3 months. a XRD patterns and b–d Raman spectra.

preferential dissolution of iron during the corrosion. Cr enrichment in the CPL can facilitate refinement of the corrosion product particles and enhancement in the compactness of the CPL[25,26], thereby playing a crucial role in inhibiting further corrosion of the steel.

Composition of corrosion products

A change in the corrosion environment may cause differences in the components and structures of the CPL, considerably affecting the corrosion and hydrogen permeation behaviour of the steel. Figure 4a shows the XRD patterns of the corrosion products formed on the coupon surfaces. All the corrosion products formed in the tidal zone had the same components, among which magnetite (Fe_3O_4), lepidocrocite (γ-FeOOH), akaganeite (β-FeOOH), and goethite (α-FeOOH) were the main components. Fe_3O_4 and γ-FeOOH were the main components of the corrosion products, according to the intensity and number of diffraction peaks. Because α-FeOOH is stable oxide, it can compact the CPL, thereby protecting the steel matrix and inhibiting corrosion[27]. However, β-FeOOH, whose formation is associated with a high concentration of Cl^- in the external environment, can alter the structure of the CPL and provide additional channels for easy penetration of corrosive substances, thereby promoting corrosion[5,27,28]. The results of Raman spectroscopy, which is an important technique for characterising the composition of substances, indicated the presence of Fe_3O_4 (characteristic peak at 675 cm^{-1}), β-FeOOH (characteristic peaks at 312 and 392 cm^{-1}), and ferrihydrite ($Fe_5HO_8 \cdot 4H_2O$, characteristic peaks ranging 1380–1600 cm^{-1}) in the corrosion products[29], as shown in Fig. 4b–d. In particular, sulfate green rust ($GR(SO_4^{2-})$) and ferrous

sulfide (FeS), whose respective characteristic peaks are 217 and 282 cm^{-1}, were present in the corrosion products formed at the LTL[30,31], as shown in Fig. 4d.

Electrochemical corrosion behaviour

Figure 5 and Supplementary Fig. 2 show the EIS results of the AISI 4135 steel after the field exposure test. According to the EIS results (Fig. 5a–c), the diameters of the capacitive arcs for the corroded samples placed at the HTL and MTL increased with increasing exposure time, whereas the diameter of the capacitive arcs for the corroded sample placed at the LTL did not consistently vary with increasing exposure time. A compressed semicircle and a diffusion tail were observed in the low-frequency region of the Nyquist plot, which are attributed to the surface roughness or heterogeneities at the metal–electrolyte interface and the diffusion barrier caused by the corrosion products, respectively[32–34]. Two time constants can be distinguished in the Bode plot (Supplementary Fig. 2); thus, the equivalent circuit $R_s(Q_r(R_r(Q_{dl}(R_{ct}Z_w)$ was initially used for fitting the EIS data. However, the quality of the fit was poor. Based on the layered structure of the CPL observed in Fig. 3, the equivalent electrochemical circuit was fine-tuned by replacing the capacitance and resistance of the entire CPL (Q_r, R_r) with the corresponding capacitances and resistances of the outer (Q_{or}, R_{or}) and inner CPLs (Q_{ir}, R_{ir}). Subsequently, the equivalent circuit shown in Fig. 6 was used for the data fitting, and the fitting parameter results are listed in Table 1. The polarisation resistance R_p ($R_{or} + R_{ir} + R_{ct}$), shown in Fig. 5d, indicates that the polarisation resistance of the steel placed at the HTL and MTL continuously increased during the exposure period, whereas that of the steel placed at the LTL first increased and then decreased. According to
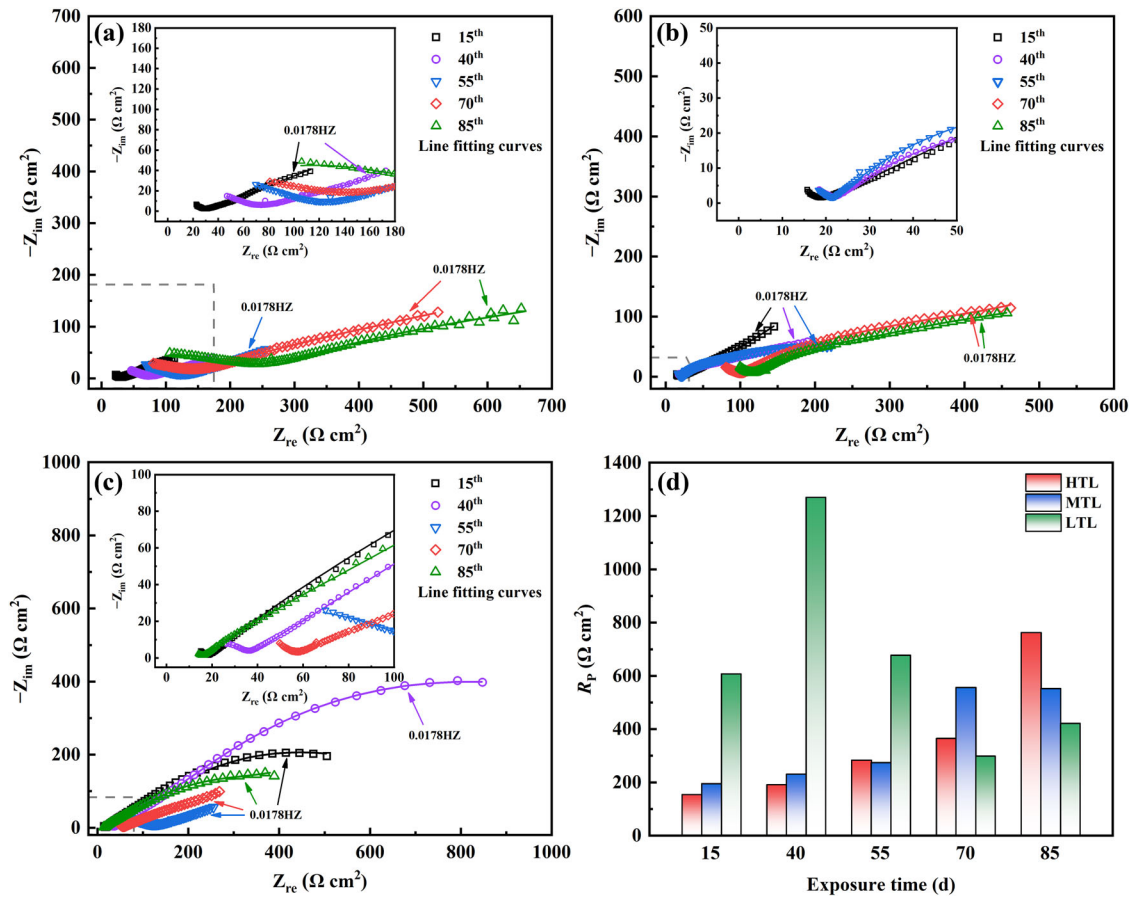
Fig. 5 EIS of the AISI 4135 steel samples after exposure to the tidal zone. Nyquist diagrams of the AISI 4135 steel samples after exposure to the **a** HTL, **b** MTL, **c** LTL for various periods and **d** calculated polarisation resistance results. The corresponding Bode diagrams can be found in Supplementary Fig. 2.
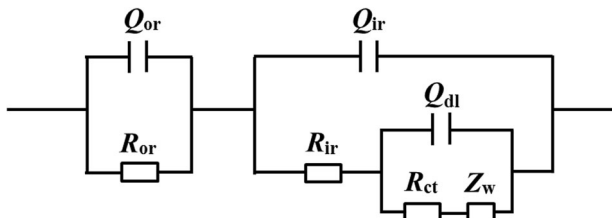

Fig. 6 Electrochemical equivalent circuit used for fitting the EIS data. Q_{or} and R_{or} are the capacitance and resistance of the outer CPL, respectively; Q_{ir} and R_{ir} are the capacitance and resistance of the inner CPL, respectively; Q_{dl} is the electric double layer capacitance; R_{ct} is the charge transfer resistance; and Z_w is the Warburg diffusion impedance.

the negative relationship between the polarisation resistance and corrosion rate, the continuous increase in the polarisation resistance of the steel placed at the HTL and MTL indicates a continuous decrease in the corrosion rate. Without considering the influence of other factors, the polarisation resistance of steel is mainly determined by the CPL formed on the surface and its accompanying effects, such as inhibition of mass transport of oxygen[35]. Accordingly, the increase and decrease in the polarisation resistance of the steel placed at the LTL may be related to the peeling and reformation of the CPL, respectively, which is confirmed by the changes in the resistance of the CPL R_r ($R_{or} + R_{ir}$), as shown in Table 1.

Figure 7a shows the corrosion morphologies of the AISI 4135 steel samples after exposure to the tidal zone for 3 months. The sample placed at the MTL was significantly affected by biofouling; almost the entire sample surface was covered by barnacles and oysters. Fouling organisms that attach to the steel surface play an important role in the corrosion, e.g., by promoting the localised corrosion or crevice corrosion of the steel[13,14]. Therefore, the corrosion of steel in outdoor marine environments is affected by not only corrosion products but also other factors such as biofouling and inorganic sediments, significantly differing from that in indoor simulated tests. Figure 7b displays the polarisation curves of the steel samples after exposure to the tidal zone for 3 months. Compared with the current of the original sample, referred to as 'blank control', the anodic current of the corroded steel samples was lower, whereas the cathodic current was significantly higher. This indicates that the CPL inhibited the AD reaction of iron and promoted the cathodic reaction; the higher the position of the steel sample in the tidal zone, the stronger the inhibiting and promoting effects of the formed CPL, respectively. The corrosion potential (E_{corr}) and corrosion current density (I_{corr}) of the electrode samples in the tidal zone were calculated using the Tafel extrapolation method, and the results are shown in Table 2. The I_{corr} results showed that the samples placed at the HTL and MTL had higher corrosion rates than the sample placed at the LTL. In other words, the higher the position of the sample in the tidal zone, the higher the corrosion rate, indicating that the dry/wet ratio determined by the sample location in the tidal zone governs the corrosion of the steel. Furthermore, the hydrogen evolution potential (E_H) of the exposed steel samples, especially the sample placed at the HTL,

Table 1. Fitted EIS results of the AISI 4135 steel samples after exposure for different periods at different locations in the tidal zone.

Exposure site	Exposure time (d)	Q_{or} (×10⁻³)	n	R_{or}	Q_{ir} (×10⁻⁶)	n	R_{ir}	Q_{dl} (×10⁻³)	n	R_{ct}	Z_w (×10⁻³)	χ^2 (×10⁻⁵)	R_r
HTL	15	1.35	0.66	1.2	1.00	0.70	25.7	19.70	0.27	127.1	2.8	12.65	26.9
	40	5.02	0.22	53.7	1.95	0.63	53.1	20.00	0.48	84.4	69.0	6.68	106.8
	55	3.57	0.28	34.1	2.53	0.58	94.6	13.06	0.24	154.5	2.0	4.42	128.7
	70	2.40	0.44	14.8	2.66	0.56	96.0	3.63	0.18	254.2	0.5	2.25	110.8
	85	6.04	0.30	190.3	5.80	0.50	182.0	4.20	0.18	390.2	0.7	8.41	372.3
MTL	15	10.21	0.42	5.8	2.05	0.67	17.7	13.32	0.44	171.4	15.1	19.51	23.5
	40	3.38	0.54	59.3	4.96	0.59	22.0	16.39	0.57	149.4	74.2	3.38	81.3
	55	2.54	0.68	31.9	2.12	0.65	21.2	6.97	0.47	221.0	85.9	4.89	53.1
	70	2.74	0.42	347.7	3.32	0.51	98.9	34.84	0.76	109.7	39.9	2.60	446.6
	85	2.27	0.45	247.9	1.51	0.54	114.7	22.87	0.69	189.6	52.7	3.40	362.6
LTL	15	19.18	0.86	240.2	3.44	0.64	18.0	3.87	0.51	349.2	27.1	31.17	258.2
	40	3.39	0.43	376.4	3.31	0.62	34.7	7.23	0.79	859.5	34.4	3.89	411.1
	55	3.91	0.46	435.5	1.13	0.70	23.6	22.37	0.98	218.2	34.9	10.12	459.1
	70	5.93	0.38	116.9	1.02	0.62	55.1	17.71	0.67	126.6	32.7	2.70	172.0
	85	4.40	0.49	120.9	1.79	0.67	15.4	9.28	0.75	285.5	33.2	11.42	136.3

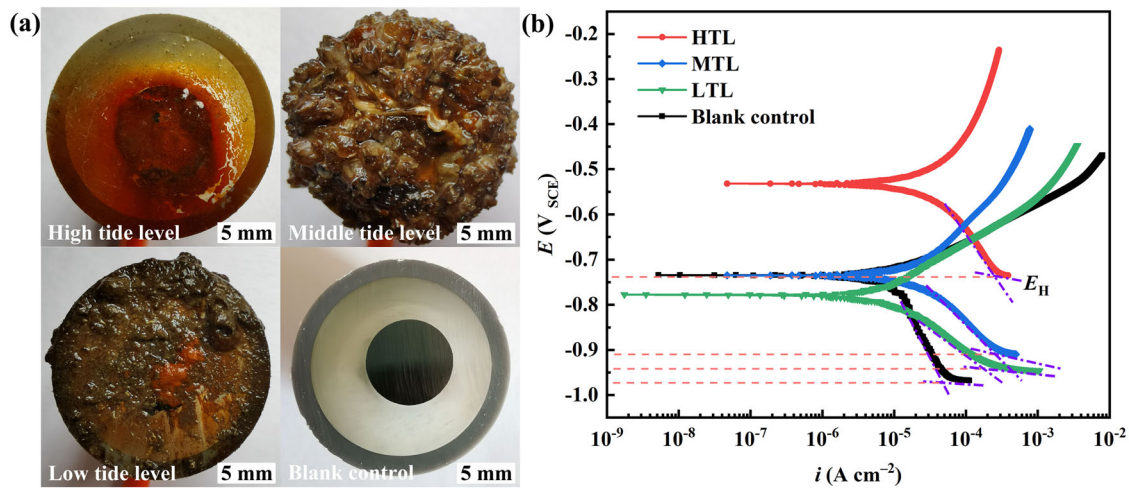The units of capacitance and resistance are Ω cm⁻² s⁻ⁿ and Ω cm², respectively.

Fig. 7 Potentiodynamic polarisation of the AISI 4135 steel samples in natural seawater. a Macro-morphologies and **b** polarisation curves of the AISI 4135 steel samples after exposure to the tidal zone for 3 months.

experienced a more positive shift than the blank control sample. The apparent positive shift in E_H is associated with the formation of corrosion products on the steel surface and is theoretically conducive to hydrogen permeation into the steel.

Results of in situ hydrogen permeation test

The hydrogen permeation devices experienced different degrees of corrosion after exposure to the tidal zone for 100 d, as shown in Fig. 8a. All the hydrogen permeation devices were affected by biofouling, especially the device placed at the MTL. The total anodic polarisation current (i_a) of the hydrogen permeation device, environmental temperature, and tidal data were continuously recorded in real time during the exposure period, and the hydrogen permeation current (i_h) was derived from the recorded i_a using Eq. (1):

$$i_h = i_a - i_b \tag{1}$$

where i_a represents the total anodic polarisation current and i_h and i_b represent the hydrogen permeation and background currents, respectively.

Figure 8b–d shows the changes in the ambient temperature and hydrogen permeation current density (j_h) for the devices placed at the HTL, MTL, and LTL from 5 to 7 August 2020, respectively; the tidal changes are also shown. The effect of tides on hydrogen permeation could be observed prominently. The hydrogen permeation current of the device placed at the HTL increased almost continuously in the submerged state, whereas the hydrogen permeation current of the device placed at the MTL decreased almost continuously in the drying state. In addition, the hydrogen permeation currents of the devices placed at the MTL and LTL always changed non-monotonically in the submerged state. Therefore, the hydrogen-permeation-current trend of the samples varied with their positions in the tidal zone, signifying that the hydrogen permeation current was affected by not only tides but also other factors. In our previous study, we determined a positive correlation between the hydrogen permeation current of the steel and the ambient temperature under marine

atmospheric corrosion conditions[36]. There are more factors that affect the hydrogen permeation into steel in tidal zone than in atmospheric zone, e.g., tides and fouling organisms. Although the effect of temperature on the hydrogen permeation current was weak in the presence of tides, the changes in the temperature and hydrogen permeation current during the same period imply a

positive effect of temperature on hydrogen permeation, as shown in Fig. 8b–d. Since the hydrogen content in steel significantly impacts the HE, the amount of hydrogen that permeates into the steels during the exposure period must be quantified. Based on the hydrogen permeation current data collected over 100 days from the outdoor hydrogen permeation test, the hydrogen permeation flux (J), sub-surface hydrogen concentration (C_0), and diffusible hydrogen content (H_c) were calculated using Eqs. (2)–(5):

$$Q_h = \int |i_h(t)| \, dt \tag{2}$$

$$J = \frac{Q_h}{nFt} \tag{3}$$

$$C_0 = \frac{J \cdot L}{D_{eff}} \tag{4}$$

$$H_c = \frac{C_0 * 10^6}{\rho} \tag{5}$$

Table 2. Fitted results of the potentiodynamic polarisation curves for the AISI 4135 steel samples after exposure to the tidal zone for 3 months.

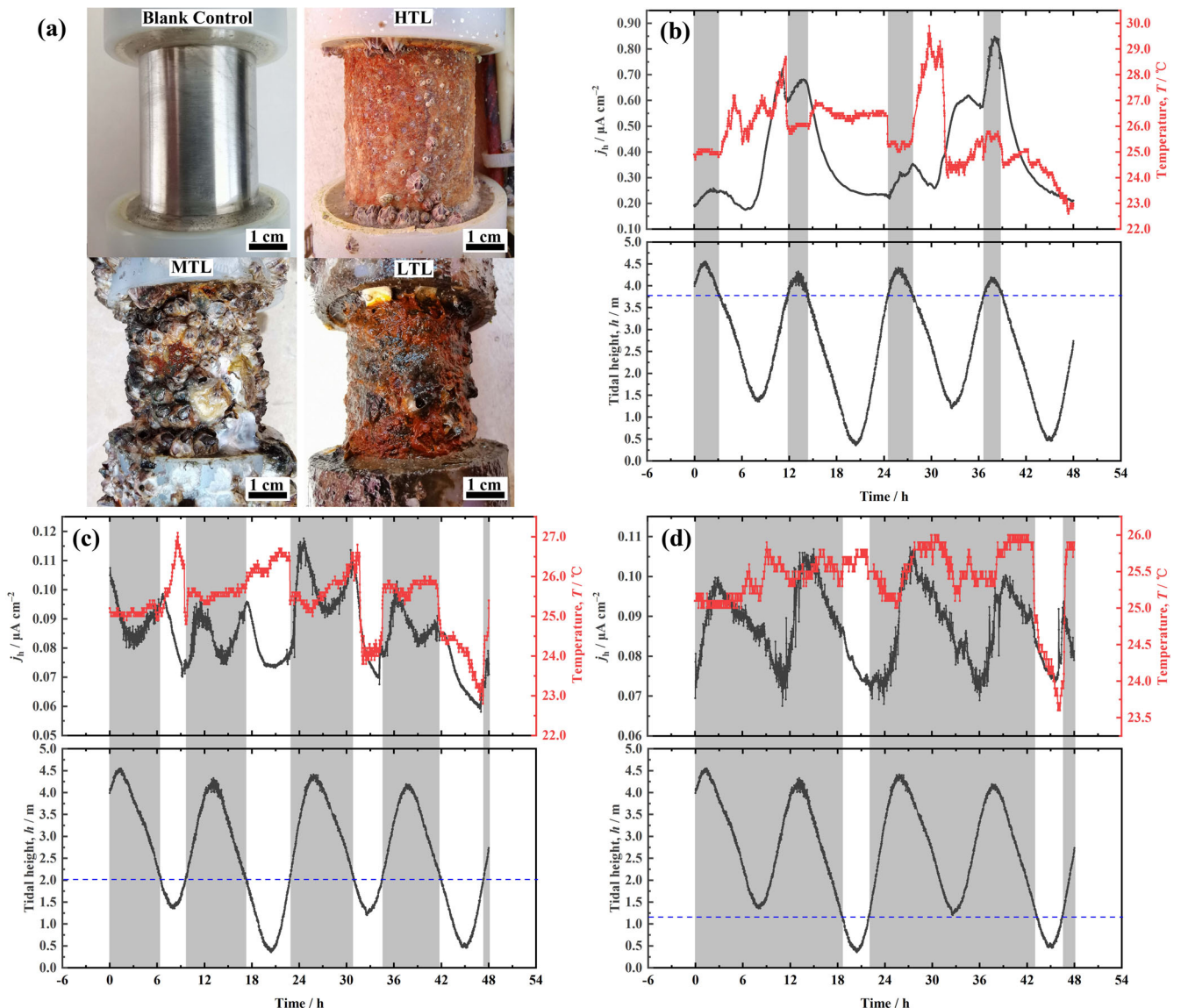| Exposure site	E_{corr}, mv	I_{corr}, µA cm^{-2}	β_a, mv dec^{-1}	β_c, mv dec^{-1}
Blank control	−742.7	9.2	79.7	−297.3
HTL	−532.3	26.1	183.8	−175.5
MTL	−733.5	19.8	160.7	−148.0
LTL	−771.1	6.4	90.9	−108.9

Fig. 8 Hydrogen permeation test results of the AISI 4135 steel samples during field exposure. a Morphologies of the hydrogen permeation devices before and after field exposure tests; variations in the ambient temperature and j_h of the devices placed at the **b** HTL, **c** MTL and **d** LTL from 5 to 7 August 2020, including the tidal changes.

Table 3. Calculated hydrogen permeation parameters for the AISI 4135 steel samples in the tidal zone, including the average hydrogen permeation current density (j_{ah}), hydrogen permeation flux (J), sub-surface hydrogen concentration (C_0), and diffusible hydrogen content (H_c).

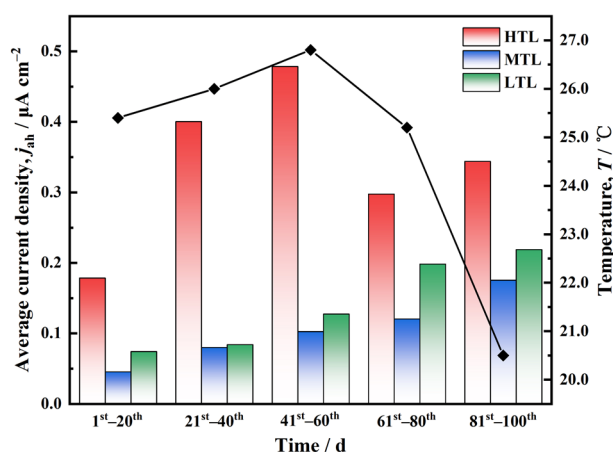| Exposure site	j_{ah}, μA cm^{-2}	$J \times 10^{-12}$, mol cm^{-2} s^{-1}	$C_0 \times 10^{-7}$, mol cm^{-3}	$H_c \times 10^{-2}$, wt ppm
HTL	0.35	3.63	4.40	5.60
MTL	0.11	1.12	1.35	1.72
LTL	0.14	1.51	1.83	2.33

Fig. 9 Average hydrogen permeation current density (j_{ah}) of the AISI 4135 steel samples and the ambient temperature for different exposure time periods. These average data were calculated for the data collected from the electrochemical hydrogen permeation test conducted from 6 July to 12 October 2020.

where Q_h is the amount of hydrogen permeation charge, L is the wall thickness of the hydrogen permeation device, F is the Faraday constant (96,485 C mol^{-1}), n is the number of electrons participating in the hydrogen reduction reaction, D_{eff} is the effective hydrogen diffusion coefficient (4.13×10^{-7} cm^2 s^{-1}, as determined using the breakthrough-time method), and ρ is the density (7.85 g cm^{-3} for steel). The calculated results are listed in Table 3. The H_c of the device placed at the HTL was approximately 3 and 1.5 times the H_c of the devices placed at the MTL and LTL, respectively, indicating that a higher dry/wet time ratio is more favourable for hydrogen permeation.

Figure 9 shows the variations in the average hydrogen permeation current density (j_{ah}) of the devices exposed to the tidal zone for different exposure time periods from 6 July to 12 October 2020. In the early stage of the exposure test, both the ambient temperature and j_{ah} increased with increasing exposure time. In the latter stage of the exposure test, the ambient temperature of the test sea area gradually decreased but the j_{ah} still increased with increasing exposure time. The variation characteristic of the hydrogen permeation current is contrary to that of the corrosion rate, with respect to the exposure time (Fig. 5d). This indicates the positive correlation between the hydrogen permeation and corrosion of steel, which was discussed in previous studies[18,21], is determined by not only the corrosion rate of steel but also other factors such as the presence of fouling organisms and development of the CPL.

Results of the SSRT

An SSRT was performed on the tensile samples placed at different locations in the tidal zone for 100 days to investigate the SCC behaviour of AISI 4135 steel; the stress–strain curves are shown in Fig. 10a. The results showed that the yield strength (σ_y), tensile strength (σ_t), and ductility of the AISI 4135 steel samples decreased by different degrees after exposure to the tidal zone. The specific values of the aforementioned parameters and the calculated elongation loss (I_δ) and reduction-in-area loss (I_ψ) are shown in Fig. 10b, c. In many studies[7,37], I_δ has been used as the SCC susceptibility index for characterising the sensitivity of SCC during crack propagation (influenced by the cracks and defects inside the steel); I_ψ has been used as the HE index for characterising the dislocation and deformation of steel (influenced by the internal hydrogen content). The tensile sample placed at the HTL had the largest I_δ and I_ψ values; the I_δ and I_ψ values of the samples placed at the MTL and LTL were significantly smaller. Accordingly, these results indicate that the AISI 4135 steel sample placed at the HTL had high SCC and HE susceptibilities, whereas the AISI 4135 steel samples placed at the MTL and LTL had low SCC and HE susceptibilities.

The scanning electron micrographs of the fracture surface and side surface of tensile samples are shown in Fig. 11. Figure 11a1 shows a typical cup-and-cone fracture of the blank control sample, which undergone significant reduction in the area of the fracture surface; the cup-and-cone fracture consisted of two regions, namely, the central region (marked as A) and the shear lips (marked as B). Figure 11a2, a3 shows that the central region was rough, with hollow and tear cracks, indicating localised plasticity and ductile tearing characteristics. An enlarged view of the central region reveals that the fracture surface was mainly composed of numerous dimples and cracks caused by micro-void coalescence (MVC)[38], indicating typical ductile fracture characteristics (Fig. 11a4). In addition, numerous micro-cracks were present on the side surface of the sample, implying highly localised plasticity near the fracture (Fig. 11a6). A little necking was observed on the fracture surface of the tensile sample placed at the HTL, as shown in Fig. 11b1, indicating high brittleness. Fig. 11b2 shows cleavage cracks at the central region of the fracture surface, indicating brittleness and the significant influence of HE, which correspond to the high embrittlement index of the sample. The higher-magnification views further confirmed the coexistence of cleavage planes, secondary cracks, and dimples in the central region (Fig. 11b3, b4), implying high brittleness and low ductility. Fig. 11b5 shows a typical shear fracture within a single plane, wherein the angle of the fracture was approximately 45° to the tensile stress direction. Therefore, the sample placed at the HTL experienced typical brittle shear fracture. The higher-magnification view reveals the presence of secondary cracks, especially cracks through the corrosion pits, on the side surface of the sample, as shown in Fig. 11b6, indicating highly localised plastic deformation around the pits[39]. The fracture morphologies of the samples placed at the MTL and LTL show features similar to those of the blank control sample—cup-and-cone fracture, significant necking, and numerous dimples—indicating high ductility, as shown in Fig. 11c1–c6 and d1–d6. Although the fracture surfaces consisted mostly of MVC dimples, some secondary cracks were also observed on the fracture surface, as shown in Fig. 11c2–c4, d2–d4. The formation of secondary cracks may be related to hydrogen enrichment at the interfaces and boundaries; hydrogen is prone to getting trapped at ferrite–pearlite interfaces, where the presence of supersaturated hydrogen is sufficient to induce micro-cracks[40,41]. This indicates that the fracture was moderately influenced by hydrogen, and the influence of hydrogen was consistent with the slight reduction in steel ductility, as shown in Fig. 10b. The criss-cross bands on the sample surface in the
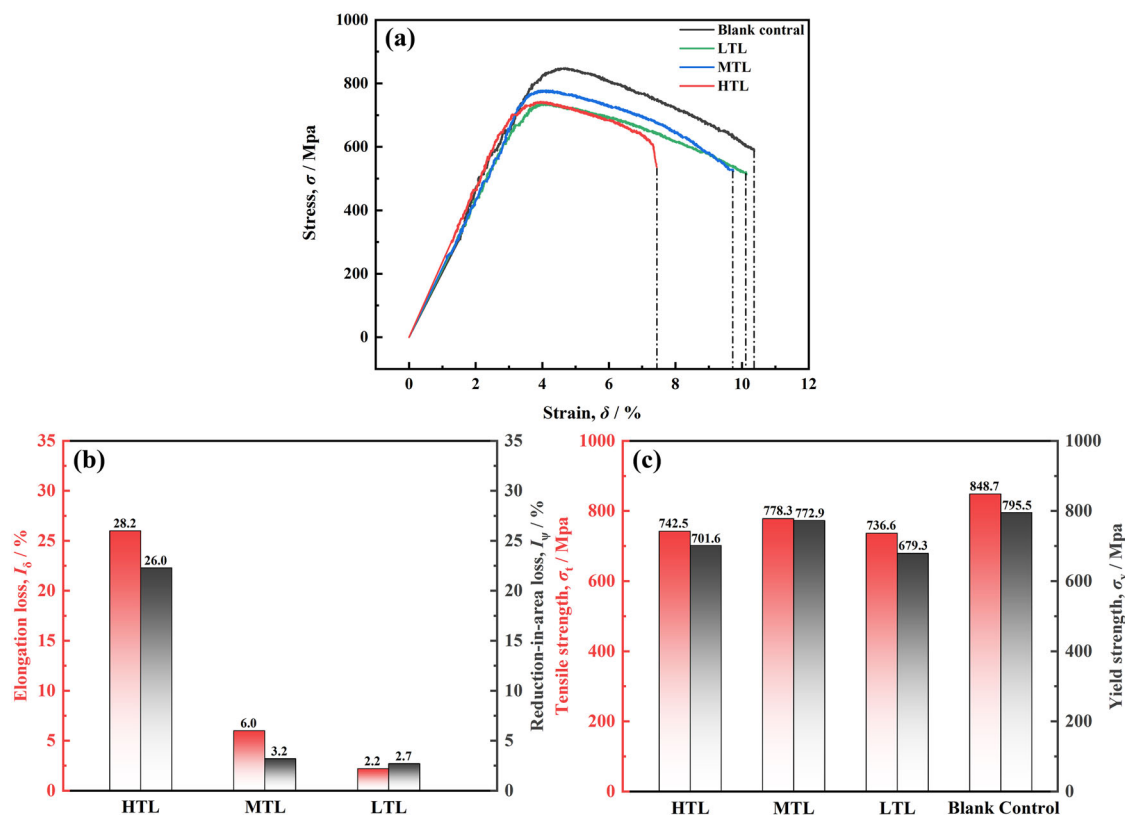
Fig. 10 Results of SSRT for the AISI 4135 steel samples after exposure to the tidal zone for 100 days. a Stress–strain curves, **b** elongation loss (l_δ) and reduction-in-area loss (l_ψ), and **c** tensile strength (σ_t) and yield strength (σ_y).

necked region of the fracture were identified as shear bands (Fig. 11c6, d6) since they were oriented 45° to the tensile stress direction and parallel to the maximum shear stress direction. However, no surface cracks were observed on the sample surface in the necked region of fracture. The shear bands in the necked region, especially near the fracture, are attributed to strain localisation due to dislocation-driven plastic deformation of metals[42], indicating the prevalence of high plastic strain. The as-observed shear bands and shear lips indicate that the final fracture of the samples was caused by the shear stress.
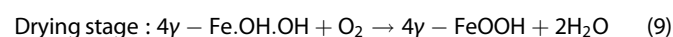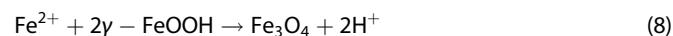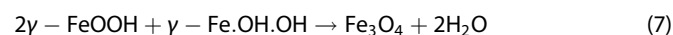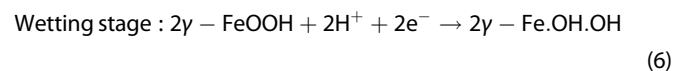
DISCUSSION

### Corrosion mechanism of AISI 4135 steel in the marine tidal zone

Tidal cycles can significantly impact steel corrosion via controlling cyclic drying/wetting of the steel surfaces. The corrosion of steel in a single tidal cycle can be divided into two stages: the corrosion under a thin electrolyte layer (TEL) when exposed to a marine atmosphere and the corrosion under seawater immersion conditions. In the primary stage of corrosion, the main electrochemical reactions of AISI 4135 steel are the AD of iron and cathodic oxygen reduction, resulting in the formation of $Fe(OH)_2$[43–45]. The initial corrosion product, $Fe(OH)_2$, is unstable and can be easily transformed into iron oxyhydroxides (FeOOH) in the presence of oxygen[46]. During the immersion stage, i.e. when the steel sample is immersed in seawater, the corrosion of steel occurs via a typical oxygen-absorbing corrosion mechanism[5,47].

Compared to the corrosion of steel under immersion conditions, the corrosion of steel under TEL conditions is more complex. First, oxygen is highly prone to diffusion through the TEL to the steel surface, thereby facilitating the occurrence of the aforementioned reactions. Second, the corrosion of steel covered by a CPL under

wet–dry cycle conditions can be divided into three stages—wetting of the dry surface, wet surface, and drying of the wet surface[48,49]—during which the corrosion products undergo oxidation–reduction–re-oxidation cycles, as follows[50–52]:

$$\text{Wetting stage}: 2\gamma - FeOOH + 2H^+ + 2e^- \rightarrow 2\gamma - Fe.OH.OH \tag{6}$$

$$2\gamma - FeOOH + \gamma - Fe.OH.OH \rightarrow Fe_3O_4 + 2H_2O \tag{7}$$

$$Fe^{2+} + 2\gamma - FeOOH \rightarrow Fe_3O_4 + 2H^+ \tag{8}$$

$$\text{Drying stage}: 4\gamma - Fe.OH.OH + O_2 \rightarrow 4\gamma - FeOOH + 2H_2O \tag{9}$$

$$4Fe_3O_4 + O_2 \rightarrow 6\gamma - Fe_2O_3 \tag{10}$$

When the CPL is again wetted by seawater, γ-FeOOH and γ-Fe_2O_3 are reduced to γ-Fe.OH.OH and Fe_3O_4, respectively, which is correspondingly shown in Eqs. (6) and (11).

$$4\gamma - Fe_2O_3 + Fe^{2+} + 2e^- \rightarrow 3Fe_3O_4 \tag{11}$$
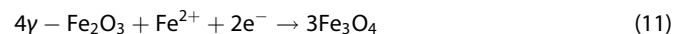
The electrons required for Eqs. (6) and (11) are provided by the AD of iron; thus, the corrosion of steel can be catalysed by the oxidation–reduction–re-oxidation cycles of the corrosion products under TEL conditions. The higher corrosion rate of steel under wet–dry cycle conditions than that under immersion conditions[5,53] and the high contents of γ-FeOOH and Fe_3O_4 in the corrosion products (Fig. 4) support the view of the occurrence of these catalytic cycles during the corrosion of steel under TEL conditions. Therefore, the dry/wet time ratio determines the corrosion rate of steel in tidal zone, and a higher time ratio leads to faster corrosion, as shown in Table 2.

As the exposure time increased, the CPL on the steel surface gradually thickened, thereby restricting ion diffusion to a certain
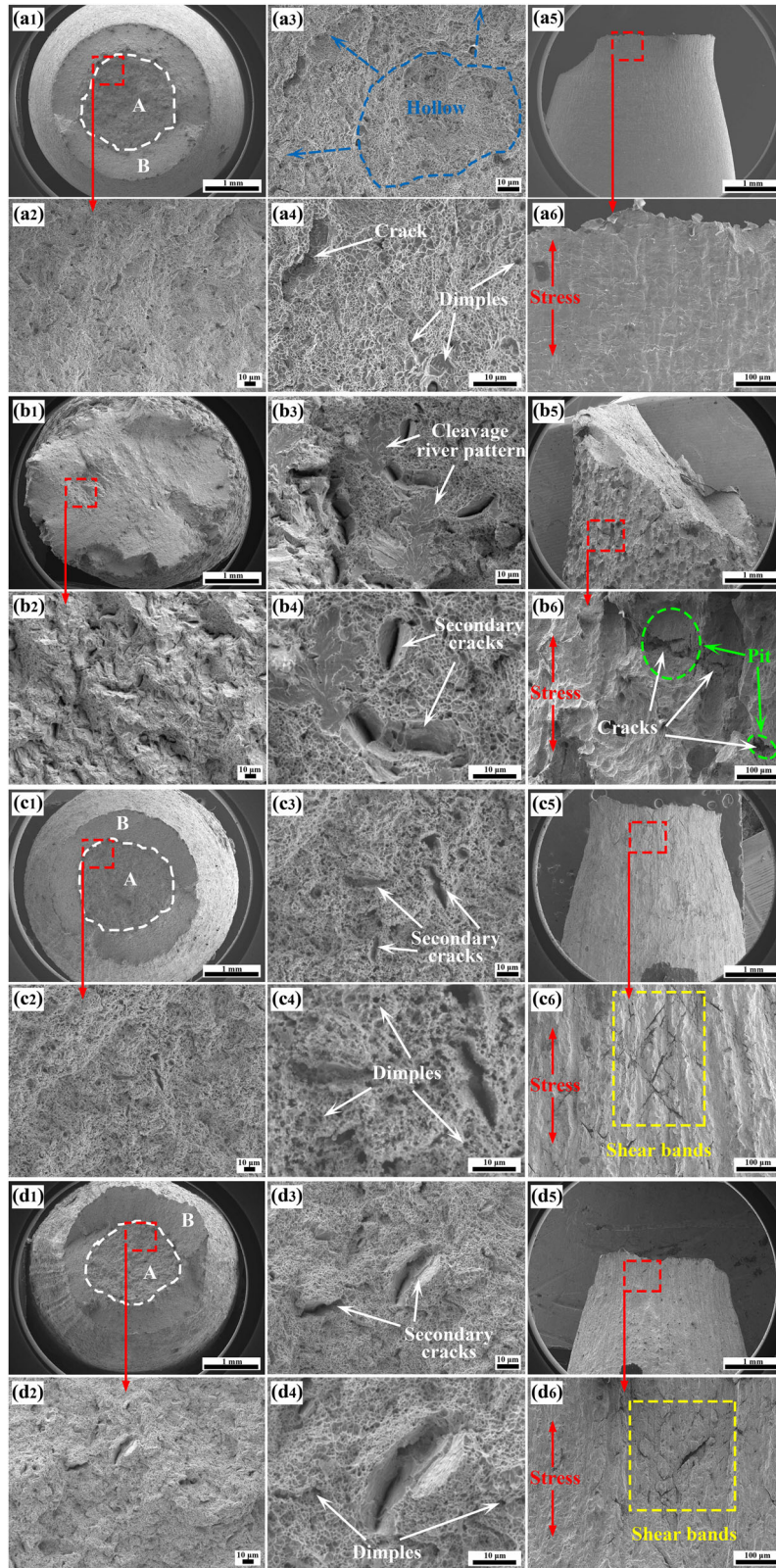
Fig. 11 SEM images of the fracture and side surfaces of the AISI 135 steel tensile samples after the SSRT. a1–a6 blank control tensile sample and tensile samples placed at the **b1–b6** HTL, **c1–c6** MTL, and **d1–d6** LTL. The corrosion products on the sample surface were removed using a rust-cleaning solution prior to the side characterisation of the sample.
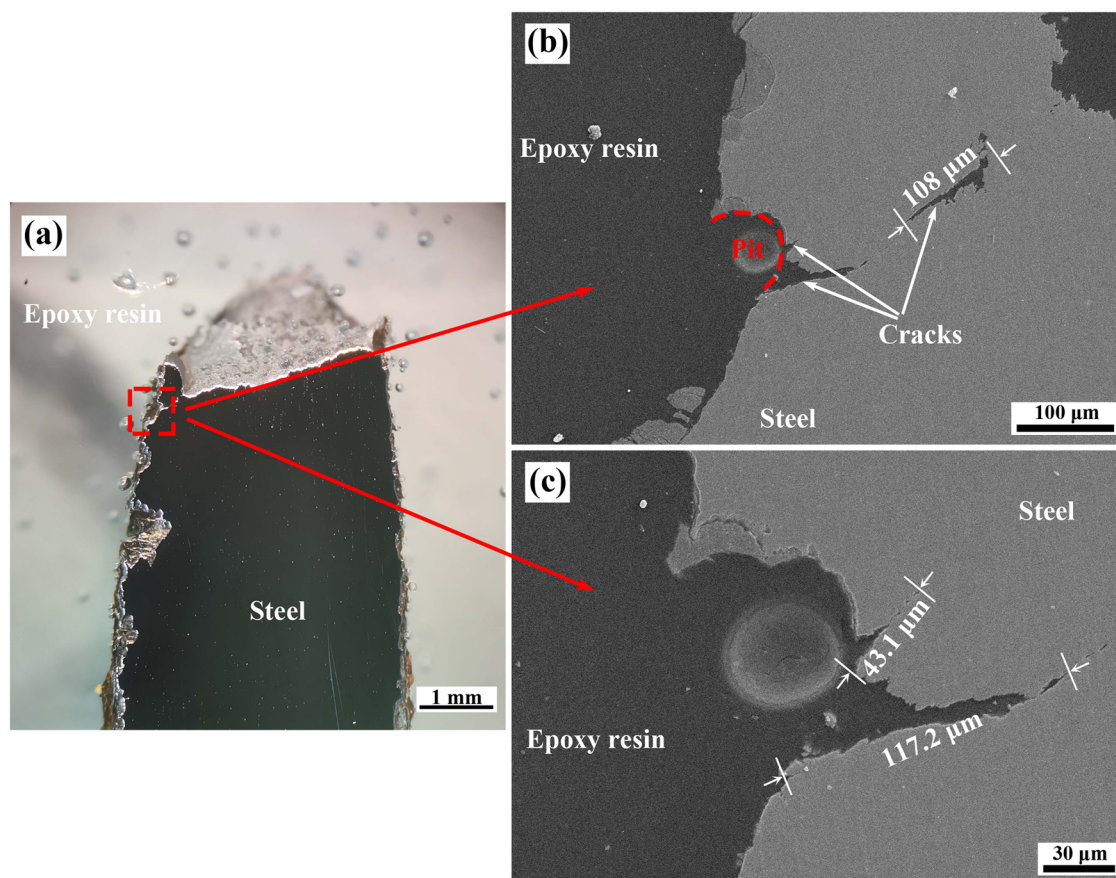
Fig. 12 Cross-sectional morphologies of the fractured tensile sample placed at the HTL. a OM image and **b, c** SEM images. SEM images show the cracks initiated at the corrosion pit.

extent. In addition, the relatively unstable as-formed rust phases initially tend to transform into chemically stable rust phases, such as α-FeOOH, which can decrease the electrical conductivity of the CPL and inhibit the electrochemical or chemical reactions on the layer surface[54]. Both the above-mentioned factors decrease the corrosion rate of steel with increasing exposure time, as shown in Fig. 5d.

Under TEL conditions, the salt concentration of the electrolyte layer in different regions of the steel surface changes to varying degrees with the evaporation of water, which is conducive to the formation of localised corrosion cells, thereby initiating localised corrosion (or pitting corrosion). In addition, although the corrosion products continuously produced by the above-mentioned reactions improved the protection ability of the CPL (Table 1) and decreased the overall corrosion rate of the steel (Fig. 5d), they significantly accelerated the localised corrosion below the CPL of the steel. Moreover, the CPL was not compact (Fig. 3); Cl^- could penetrate the CPL and concentrate on the steel surface, facilitating the AD of local active sites and the hydrolysis of Fe^{2+} and Fe^{3+}. Furthermore, the CPL could block the outward diffusion of cations from the corrosion pits to a certain extent; to maintain the electroneutrality of the electrolyte, Cl^- would be enriched in the corrosion pits. Therefore, an 'autocatalytic effect' caused by the Cl^- enrichment could occur inside the pits, which promoted the further development of corrosion pits[7,21].

It is more difficult for cations, such as Fe^{2+} and Fe^{3+}, to diffuse outward under TEL conditions than under immersion conditions because of the smaller internal–external ion concentration gradient of the electrolyte with respect to the CPL. Therefore, pitting corrosion is more likely to occur under TEL conditions, as confirmed in many studies[5,7]. Yu et al.[55] even showed that pitting corrosion of

X65 pipeline steel only occurs under alternating dry/wet conditions, whereas general corrosion occurs under immersion conditions. Therefore, the dry/wet time ratio determined by the location of the steel in the tidal zone crucially impacts the pitting corrosion of the steel in the tidal zone, and a higher time ratio results in more severe pitting corrosion, as shown in Figs. 1 and 2.

Hydrogen permeation mechanism of AISI 4135 steel in the marine tidal zone

In general, hydrogen in the interior of steel can be divided into two types: endogenous hydrogen introduced into the steel during metal smelting, electroplating, and pickling, and exogenous hydrogen generated and absorbed during the corrosion, as a part of the service life. The resulting HE are referred to as internal HE and hydrogen environment embrittlement, respectively[56]. Hydrogen permeation due to the corrosion of steel has been widely studied and reported over the past few decades; hydrogen ions produced by the hydrolysis of corrosion products have been demonstrated as the main source of hydrogen absorbed in steels[18,21]. These hydrogen ions can permeate steel by participating in the cathodic reactions of steel corrosion. Hydrogen can permeate into steel either directly under acidic conditions or indirectly under neutral or alkaline conditions via an intermediate adsorbed state, as follows[57–59]:

$$H^+ + M + e^- \quad MH_{abs} \tag{12}$$

$$H^+ + M + e^- \quad MH_{ads} \rightarrow MH_{abs} \tag{13}$$

where M is the steel matrix, MH_{ads} is the adsorbed hydrogen atoms on the steel surface, and MH_{abs} is the absorbed hydrogen atoms in the sub-surface of the steel.
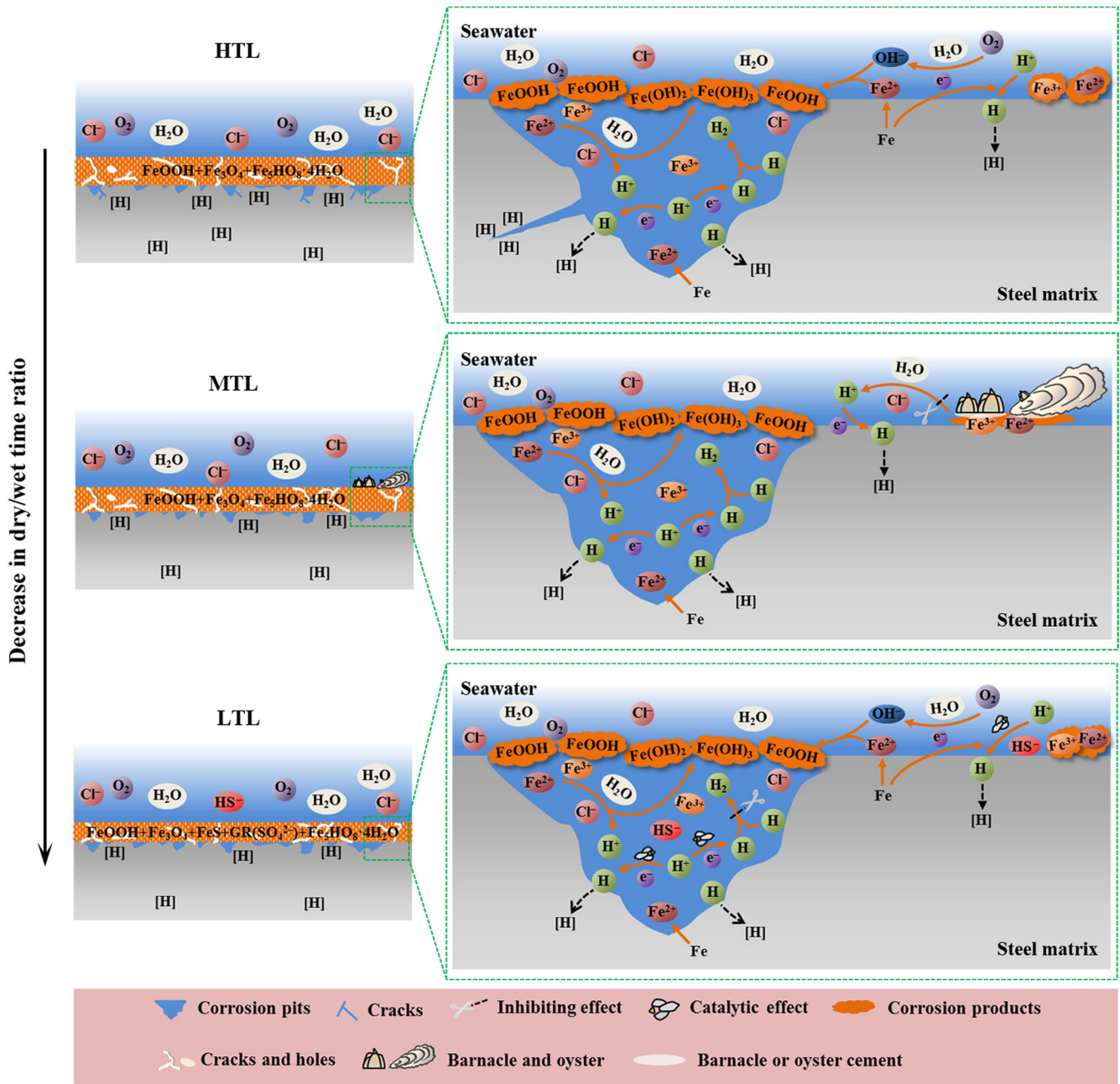
Fig. 13 Schematics of the corrosion, hydrogen permeation, and SCC behaviours of AISI 4135 steel at different locations in the tidal zone. The figure highlights the prominent roles of the corrosion pits, biofouling, and sulfides in SCC of the AISI 4135 steel samples placed at the HTL, MTL, and LTL, respectively.

It can be inferred from Eqs. (12) and (13) that the pH of the electrolyte below the CPL has decisive impact on the hydrogen permeation into steel under natural corrosion conditions. As discussed in the section 'Corrosion mechanism of AISI 4135 steel in the marine tidal zone', Cl^- can promote the hydrolysis of corrosion products and lead to further acidification of the electrolyte below the CPL, and the pH can drop to 3 with the evaporation of water under TEL conditions[21,60].

According to the Nernst equation, the equilibrium potential of the hydrogen evolution reaction [$E_{e(H_2/H^+)}$] is as follows (at 25 °C):

$$E_{e(H_2/H^+)} = -0.0591 pH \tag{14}$$

Therefore, when the electrolyte pH is approximately 3, the $E_{e(H_2/H^+)}$ is −418 mV [vs saturated calomel electrode (SCE)], which

is significantly higher (more positive) than that in natural seawater [pH = 8.0; $E_{e(H_2/H^+)}$ = −714 mV]. Accordingly, the acidification of the electrolyte due to Cl^--catalysed hydrolysis of the corrosion products can largely facilitate hydrogen permeation. In this case, a thicker CPL is theoretically more conducive to hydrogen permeation because it can provide more hydrolysable corrosion products and better block the outward diffusion of H^+, Fe^{2+}, Fe^{3+}, etc. Accordingly, it can be inferred that the intense hydrolysis of the corrosion products results in a significant decrease in the pH of the electrolyte below the CPL, which ultimately leads to the positive shift in the hydrogen evolution potential of the corroded steel samples, especially the samples placed at the HTL, as shown in Fig. 7b. Therefore, the steel sample placed at the HTL has a higher hydrogen permeation current and the hydrogen

permeation current of the samples in the tidal zone increases with increasing exposure time (Fig. 9).

The amount of hydrogen absorbed in steel is positively related to the corrosion loss of steel[18,21]; however, the inferences drawn herein from the corrosion rate and hydrogen content of the steel samples placed at the MTL and LTL indicate otherwise, as shown in Tables 2 and 3. On the one hand, this could be attributed to the difference in the metabolic activity of sulfate-reducing bacteria (SRBs). The Raman spectrum of the corrosion products for the steel sample placed at the LTL revealed high-intensity peaks of ferrous sulfide (FeS); however, FeS was not detected in the corrosion products of the steel sample placed at the MTL, as shown in Fig. 4. The formation of FeS in corrosion products is closely related to the metabolic activity of SRBs, which are typically active in the inner CPL[31]. Metabolites of SRBs, such as S^{2-} and HS^-, can catalyse hydrogen ion reduction but poison hydrogen atom recombination, thereby leading to more hydrogen permeation into steel[19,61–63]. Therefore, although the corrosion rate of the steel sample placed at the LTL was relatively low (Table 2), the positive effect of SRBs and its metabolites, especially sulfides, on hydrogen absorption in the steel increased the hydrogen content in the steel sample placed at the LTL (Table 3). On the other hand, the influence of biofouling on hydrogen permeation should also be considered. Palanichamy et al.[14] found out that the corrosion loss of steel is negatively correlated to the biomass, especially macro-fouling organisms, on the steel surface. However, the effect of macro-fouling organisms, such as oysters and barnacles, on hydrogen penetration is still unclear. Nevertheless, considering the negative effect of the cement secreted by oyster and barnacle colonies over the rusty steel surface on the hydrolysis activity of the corrosion products[64], macro-fouling may have a certain inhibitory effect on hydrogen permeation. Therefore, severe biofouling (Fig. 8a) may also be one of the reasons for the low hydrogen content of the steel sample placed at the MTL.

The above-mentioned analyses indicate that the hydrogen permeation behaviour of the AISI 4135 steel in the tidal zone is not only directly related to the corrosion of steel, including the corrosion rate and the CPL, but also directly or indirectly affected by environmental factors, especially SRBs and macro-fouling organisms. It is the influence of these external factors in the real world that may cause the results obtained under simulated experimental conditions to differ.

SCC mechanism of AISI 4135 steel in the marine tidal zone

The SSRT results show that the AISI 4135 steel samples at different locations in the tidal zone have different SCC susceptibilities, which is closely associated with corrosion, particularly pitting corrosion, and HE caused by hydrogen permeation into the steel. As analysed in the sections 'Corrosion mechanism of AISI 4135 steel in the marine tidal zone' and 'Hydrogen permeation mechanism of AISI 4135 steel in the marine tidal zone', under wet–dry cycle conditions, the synergy between the CPL and Cl⁻ led to varying degrees of pitting corrosion and hydrogen permeation of the steel samples in the tidal zone. Upon the formation of corrosion pits, acidification of the electrolyte inside the corrosion pits due to the autocatalytic effect can further accelerate local AD in the pits and facilitate hydrogen permeation into the steel through the pits[7,9]. Under tensile stress, corrosion pits can promote hydrogen-induced cracking when the sub-surface hydrogen concentration of steel reaches the critical hydrogen concentration. On the cross-section of the tensile sample placed at the HTL, cracks were observed to initiate at the corrosion pit near the fracture and propagate the interior of the sample, with the lengths of the cracks were approximately 43.1 and 117.2 μm, respectively, as shown in the optical microscopy (OM) and SEM images in Fig. 12. This leads to two inferences: first, the sub-surface hydrogen concentration of the tensile sample

placed at the HTL reached the critical hydrogen concentration, so the HE was significantly enhanced; second, the corrosion pits (or local AD) provided preferential sites for crack nucleation. The initiation and propagation of cracks on steel surfaces can be explained by the adsorption-induced dislocation emission (AIDE) mechanism[65]. Through the AIDE mechanism, the high sub-surface hydrogen concentration at high-stress-intensity-factor regions, such as corrosion pits and crack tips, can trigger the release of dislocations from the pits and crack tips, leading to crack initiation and growth and intense deformation near the crack. This is consistent with the high hydrogen concentration and stress intensity factor at the corrosion pits[66]. In addition, the macroscopically neat and smooth shear-type fracture surface and the microscopically obvious river-like patterns and secondary cracks (Fig. 11b1–b4) indicate that the interior of the steel was also significantly affected by HE, which is consistent with the high HE index of the tensile sample (Fig. 10b). In the case of high internal brittleness of the sample, surface cracks that are preferentially initiated and propagated in the corrosion pits under stress trigger brittle shear fracture of the sample placed at the HTL. Furthermore, Lynch[65] pointed out that AIDE is the dominant mechanism for the cleavage of river-like fractures, based on the features of the fracture surface such as high local plastic strain, extensive slip on planes intersecting the crack fronts, and void formation ahead of the cracks. Therefore, the high SCC susceptibility of the sample placed at the HTL is combinedly determined by localised AD and HE, and AIDE is the main HE mechanism.

Numerous shear bands and significant necking were observed on the surfaces of the tensile samples placed at the MTL and LTL, but no surface cracks were observed, as shown in Fig. 11c5–c6, d5–d6. This implies that the sub-surface hydrogen concentration of the steels did not reach the critical hydrogen concentration, which is consistent with the relatively low hydrogen content in these steel samples, as shown in Table 3. Therefore, these results indicate that corrosion pits (or localised AD) have little effect on promoting surface crack initiation, propagation and increasing the SCC susceptibility of the steel whose hydrogen content is relatively low. As stated in the section 'Results of the SSRT', the fracture surface consists of a large number of dimples caused by MVC (Fig. 11c4, d4). The MVC consists of five stages—void nucleation, void growth, void coalescence, crack propagation, and separation of the remaining ligament by shear—which are closely correlated to the central region and shear lips of the fracture surface[39]. The central region is the main region for void nucleation, growth, and coalescence and crack propagation, and the globular dimples and hollows therein suggest that tensile stress resulted in the tearing of the section via MVC. The last stage of the fracture occurred at the shear lips, which were oriented 45° to the tensile stress direction, indicating that the final fracture of the steel was caused by the shear stress (Fig. 11c1, d1). Hydrogen can decrease the shear modulus to a certain extent[67], so the relatively low hydrogen content may also play a certain role in increasing the SCC susceptibilities of the tensile samples placed at the MTL and LTL, as shown in Fig. 10b. Furthermore, the hydrogen absorbed in the steel furthered the fracture by promoting the initiation and propagation of secondary cracks within the steel, despite the low hydrogen content in the steel, as shown in Fig. 11c2–c4, d2–d4. Therefore, in the case of low internal hydrogen content, the fracture of steel under tensile stress is mainly governed by MVC and slightly impacted by HE.

Summary

The results and analyses of this study infer that the corrosion and hydrogen permeation behaviours of AISI 4135 steel vary with the position of the steel in the tidal zone, thereby leading to differences in the SCC behaviour and mechanism of the steel. The main differences are summarised in Table 4 and depicted in

Table 4. Main differences between the external environment and corrosion, hydrogen permeation, and SCC behaviours of the AISI 4135 steel samples at different locations in the tidal zone.

Exposure site	Dry/wet time ratio	Biofouling	Corrosion products composition	Corrosion product layer thickness	Size of pits	Hydrogen content	SCC susceptibility
HTL	High	Slight	$FeOOH$, Fe_3O_4, $Fe_5HO_8 \cdot H_2O$	Large	Large	High	High
MTL	Medium	Severe	$FeOOH$, Fe_3O_4, $Fe_5HO_8 \cdot H_2O$	Medium	Medium	Low	Low
LTL	Low	Slight	$FeOOH$, Fe_3O_4, FeS, $GR(SO4^{2-})$, $Fe_5HO_8 \cdot H_2O$	Small	Small	Low	Low

Fig. 13. At a higher dry/wet time ratio, the steel placed at the HTL experienced more severe pitting corrosion, and a thicker CPL facilitated further hydrogen permeation. The synergy between the AD and intense hydrogen evolution reactions in the corrosion pits promoted crack initiation and propagation in the pits (Fig. 13), consequently increasing the SCC susceptibility of the steel. Biofouling is the most influential factor for the steel placed at the MTL. With decreasing dry/wet time ratio and because of the negative effect of biofouling on hydrogen permeation, the sub-surface hydrogen concentration of the steel did not reach the critical hydrogen concentration. No cracks were initiated at the corrosion pits, and the steel had a low SCC susceptibility. Although the SRBs and sulfides in the corrosion products formed on the surface of the steel placed at the LTL facilitated hydrogen permeation (Fig. 13), the internal hydrogen content of the steel still decreased with decreasing dry/wet time ratio. Therefore, no cracks were present in the corrosion pits, and the steel also had a low SCC susceptibility.

METHODS

Materials and field exposure test site

The test material used in the present study was as-received AISI 4135 steel, manufactured by Beijing Shougang New Steel Co., Ltd., P. R. China, with the following chemical composition (wt.%): 0.903 Cr, 0.509 Mn, 0.399 C, 0.293 Si, 0.204 Mo, 0.0804 Ni, 0.0146 P, 0.0144 S, and Fe balance. The yield strength, tensile strength, and elongation of steel at room temperature (20 °C) were approximately 790 MPa, 850 MPa, and 10.4%, respectively. Supplementary Fig. 3 shows the microstructure of AISI 4135 steel cut from the raw steel plate; multivariate ferrite and pearlite were present in the steel matrix, as characterised by OM[53].

Four types of steel samples (Fig. 14) were used in this study: corrosion coupons and electrode samples for the corrosion test, hydrogen permeation samples for the hydrogen permeation test, and tensile samples for the SSRT. All the samples were subjected to the same surface treatment; the final roughness was Rz1.6.

Field exposure tests were carried out in Jiaozhou Bay (36° 06′ N, 120° 10′ E), Qingdao, on the northeast coast of P. R. China. It is a trumpet-shaped semi-enclosed bay located in a typical semi-diurnal tidal sea area. The main meteorological data at the field exposure site include the atmospheric temperature (12.3 °C), relative humidity (71%), and major seawater properties, such as salinity (31.5 ppt), seawater temperature (13.7 °C), and pH (8.3); the values represented herein are mean data.

Corrosion test

The corrosion behaviour of AISI 4135 steel at different locations in the tidal zone was investigated by field exposure tests and laboratory tests. Each group of corrosion coupons and electrode samples was secured to the respective sample holder. These holders were strung together using steel wire ropes and placed at the HTL, MTL, and LTL. The HTL, MTL, and LTL were at 3.77, 1.99,

and 1.05 m in the tidal zone, respectively, in terms of the tidal records in this sea area.

To evaluate the electrochemical corrosion behaviour of steel during the field exposure tests, EIS and potentiodynamic polarisation curve tests were performed on the electrode samples using an IVIUM Vertex electrochemical workstation equipped with a three-electrode cell. In the three-electrode system, natural seawater was used as the electrolyte, a Pt foil (10 mm × 10 mm) was used as the counter electrode, and an SCE was used as the reference electrode (RE). Before each EIS test, the electrode sample was removed from the tidal zone and placed in the three-electrode cell, and the open-circuit potential (OCP) was recorded for at least 40 min. The EIS tests were then performed at an OCP with a sinusoidal amplitude of 5 mV over a frequency range of 100 kHz to 10 mHz. After the test, the electrode samples were transferred back to the tidal zone. After the last EIS test, a potentiodynamic polarisation curve test was performed on the electrode sample from −200 to +200 mV (vs OCP) at a scan rate of 0.167 mV s^{-1}, and the results were analysed using the Tafel extrapolation method.

The corrosion products collected from the recovered corrosion coupons were ground into fine powders, which were then analysed by XRD and Raman spectroscopy. XRD was performed using an Ultima IV X-ray diffractometer using Cu Kα radiation ($\lambda = 1.5406$ Å) as the target, with a voltage of 40 kV and an electrical current of 40 mA. The scan rate was 10° min^{-1}, and the scan range of the diffraction angle (2θ) was 5°–80°. Raman analysis was performed at room temperature using a Renishaw MZ20-FC micro-Raman spectrometer equipped with a diode-pumped solid-state green laser ($\lambda = 532$ nm). To prevent the phase transformation of relatively unstable corrosion products, the laser power was set to 5–10% of the maximum, and the Raman shift range was 0–1800 cm^{-1}.

After the field exposure tests, the recovered corrosion coupon was cut into two parts. One part of the coupon was completely sealed with epoxy resin and then ground and polished with SiC papers and an abrasive, respectively, to obtain a smooth cross-section for analysis. A S-3400N scanning electron microscope was used for characterising the cross-sectional morphology of the CPL, and an UltraDry EDS detector (integrated with the microscope) was used for examining the elemental distribution in the CPL. The corrosion products on the surface of the other part of the coupon were completely removed using a mixture of 20 vol% hydrochloric acid and 1 vol% hexamethylenetetramine. The corrosion morphology of the coupon was examined by CLSM (Olympus LEXT OLS5000) equipped with a semiconductor laser (405 nm) and a scanning electron microscope.

Hydrogen permeation test

A hydrogen permeation device was developed using the Devanathan–Stachurski technique for in situ monitoring of hydrogen permeation into the steel during exposure[68], as shown in Fig. 14. The hydrogen permeation device was a three-electrode cell, and the detailed structure has been described in our previous
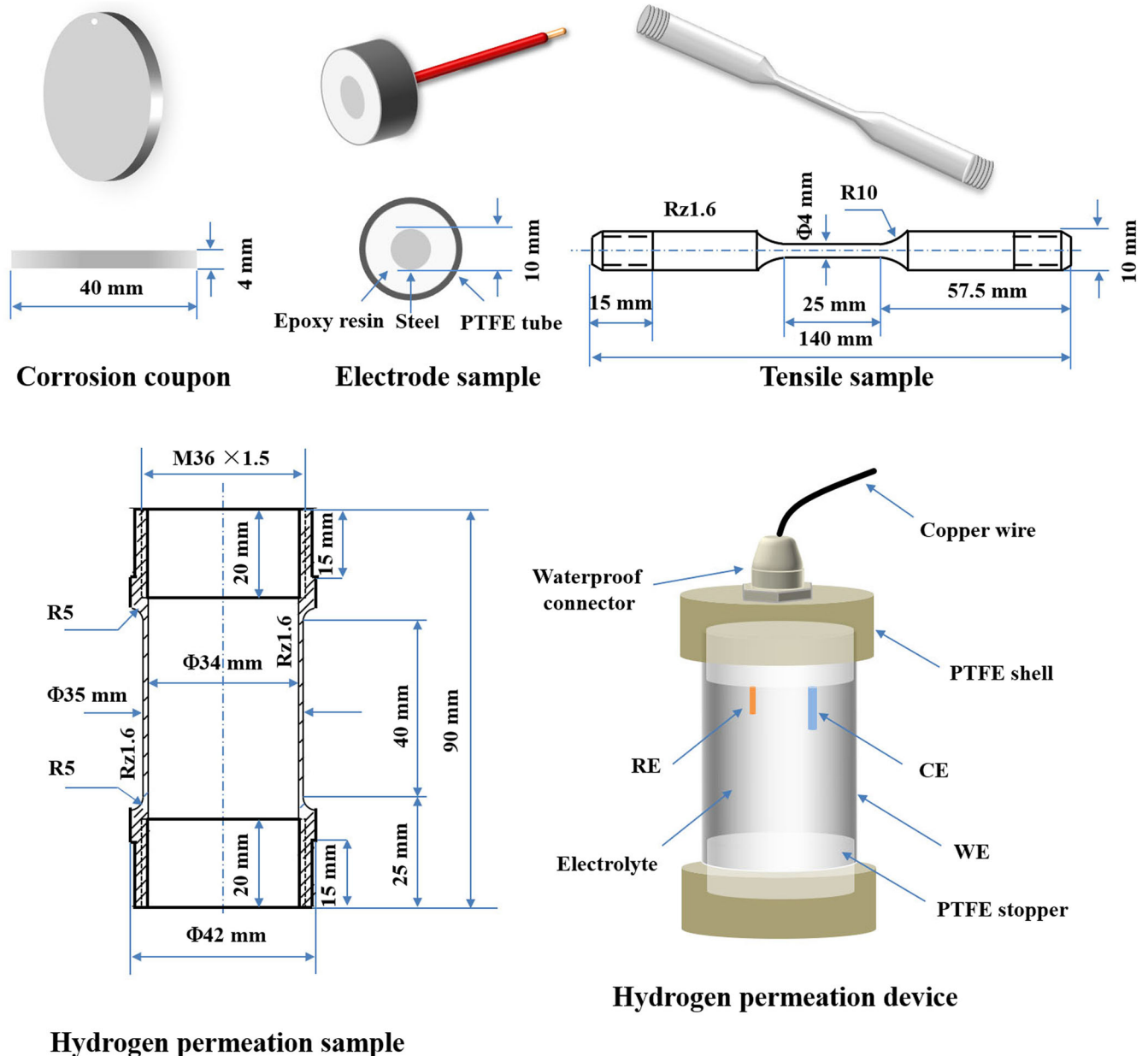
Fig. 14 Schematics of the AISI 4135 steel coupons and samples. The figure shows the corrosion coupons and electrode samples used in the corrosion test, tensile samples used in the SSRT, and hydrogen permeation samples used in the electrochemical hydrogen permeation test.

study[36]. The exterior of the device was sealed by threaded members and epoxy resin, and the exposure area on the outer surface was 43.98 cm². During the hydrogen permeation test, the entire external environment of the device functioned as the hydrogen charging chamber, whereas the device interior served as the hydrogen detection chamber.

The hydrogen permeation monitoring system implemented for the field hydrogen permeation test consisted of hydrogen permeation devices and a multi-channel potentiostat (Model PS-08, Japan) for inputting a constant polarisation potential and determining the polarisation current, respectively. Prior to the field hydrogen permeation test, the device interior was polarised at 0 mv (vs Hg/HgO/0.2 mol L⁻¹ NaOH RE) for 24 h to achieve a relatively stable low polarisation current (background current). Subsequently, the hydrogen permeation devices were placed at the HTL, MTL, and LTL using steel wire ropes, which were kept

parallel to the groups of the above-mentioned corrosion samples. Each hydrogen permeation device was connected to a channel of the potentiostat via a waterproof copper wire onshore, and the polarisation current (total anodic polarisation current) was continuously measured at a polarisation potential of 0 mV. Furthermore, the changes in the temperature and tides were monitored in real time using a temperature sensor and pressure sensor, respectively, and the data were recorded using a data logger (HIOKI MEMORY HILOGGER).

SSRT

Prior to the SSRT, the tensile samples were subjected to field exposure for 105 d. The tensile samples were fixed on sample holders, which were subsequently strung together using steel wire ropes and placed at the HTL, MTL, and LTL. The tensile samples

were completely sealed with Parafilm for waterproofing except for the testing area. The SSRT was performed at a crosshead speed of 1.25×10^{-4} mm s^{-1} (yielding a strain rate of 5×10^{-6} s^{-1}) using an SCC testing instrument equipped with an environmental chamber, as shown in Supplementary Fig. 4. During the test, the samples were immersed in natural seawater. The fracture and side surfaces of the samples were characterised by SEM (JSM-7610F) after removing the corrosion products. Subsequently, the fractured surface of the sample was sealed with epoxy resin, and the side surface was ground and polished to afford a cross-section for SEM characterisation.

DATA AVAILABILITY

The data presented in this article are available upon request to the authors.

REFERENCES

1. Zhang, T. et al. Comparison of hydrogen embrittlement susceptibility of three cathodic protected subsea pipeline steels from a point of view of hydrogen permeation. *Corros. Sci.* **131**, 104–115 (2018).
2. Huang, W. H., Yen, H. W. & Lee, Y. L. Corrosion behaviour and surface analysis of 690 MPa-grade offshore steels in chloride media. *J. Mater. Res. Technol.* **8**, 1476–1485 (2019).
3. Xie, F. et al. Stress corrosion cracking behavior induced by sulfate-reducing bacteria and cathodic protection on X80 pipeline steel. *Constr. Build. Mater.* **308**, 125093 (2021).
4. Raykar, N. R., Raman, R. K. S., Maiti, S. K. & Choudhary, L. Investigation of hydrogen assisted cracking of a high strength steel using circumferentially notched tensile test. *Mat. Sci. Eng. A Struct.* **547**, 86–92 (2012).
5. Gong, K., Wu, M. & Liu, G. X. Comparative study on corrosion behaviour of rusted X100 steel in dry/wet cycle and immersion environments. *Constr. Build. Mater.* **235**, 117440 (2020).
6. Gong, K., Wu, M. & Liu, G. X. Stress corrosion cracking behavior of rusted X100 steel under the combined action of Cl$^-$ and HSO$_3^-$ in a wet-dry cycle environment. *Corros. Sci.* **165**, 108382 (2020).
7. Liu, Z. Y., Hao, W. K., Wu, W., Luo, H. & Li, X. G. Fundamental investigation of stress corrosion cracking of E690 steel in simulated marine thin electrolyte layer. *Corros. Sci.* **148**, 388–396 (2019).
8. Hao, W. K. et al. Electrochemical characterization and stress corrosion cracking of E690 high strength steel in wet-dry cyclic marine environments. *Mat. Sci. Eng. A Struct.* **710**, 318–328 (2018).
9. Gong, K., Wu, M., Xie, F., Liu, G. X. & Sun, D. X. Effect of Cl$^-$ and rust layer on stress corrosion cracking behavior of X100 steel base metal and heat-affected zone in marine alternating wet/dry environment. *Mater. Chem. Phys.* **270**, 124826 (2021).
10. Zhou, X. B. et al. A study on corrosion of X80 steel in a simulated tidal zone. *J. Mater. Res. Technol.* **12**, 2224–2237 (2021).
11. Yu, X. M., Huang, Y. L., Yadav, A. P. & Qu, W. J. Study on the temperature dependence of pitting behavior of AISI 4135 steel in marine splash zone. *Electrochemistry* **83**, 541–548 (2015).
12. Neville, A. & Hodgkiess, T. Localised effects of macrofouling species on electrochemical corrosion of corrosion resistant alloys. *Brit. Corros. J.* **35**, 54–59 (2000).
13. Permeh, S., Lau, K., Boan, M. E. & Duncan, M. Influence of macro- and microfouling on corrosion of steel bridge piles submerged in natural waters. *J. Mater. Civil. Eng.* **33**, 04021105 (2021).
14. Palanichamy, S., Subramanian, G. & Eashwar, M. Corrosion behaviour and biofouling characteristics of structural steel in the coastal waters of the Gulf of Mannar (Bay of Bengal). *Biofouling* **28**, 441–451 (2012).
15. Tian, H. Y. et al. Electrochemical corrosion, hydrogen permeation and stress corrosion cracking behavior of E690 steel in thiosulfate-containing artificial seawater. *Corros. Sci.* **144**, 145–162 (2018).
16. Ma, H. C. et al. Stress corrosion cracking of E690 steel as a welded joint in a simulated marine atmosphere containing sulphur dioxide. *Corros. Sci.* **100**, 627–641 (2015).
17. Zhang, Y., Zheng, K. F., Zhu, J., Lei, M. & Feng, X. Y. Research on corrosion and fatigue performance of weathering steel and high-performance steel for bridges. *Constr. Build. Mater.* **289**, 123108 (2021).
18. Ootsuka, S., Fujita, S., Tada, E., Nishikata, A. & Tsuru, T. Evaluation of hydrogen absorption into steel in automobile moving environments. *Corros. Sci.* **98**, 430–437 (2015).
19. Zhu, Y., Huang, Y., Zheng, C. & Yu, Q. The hydrogen permeation investigation of API X56 steel in sea mud. *Mater. Corros.* **58**, 447–451 (2007).
20. Qu, W. et al. Effect of heat treatment on hydrogen permeation behaviour of AISI 4135 steel under splash zone conditions. *Corros. Eng. Sci. Technol.* **51**, 163–170 (2016).
21. Huang, Y. L. & Zhu, Y. Y. Hydrogen ion reduction in the process of iron rusting. *Corros. Sci.* **47**, 1545–1554 (2005).
22. de la Fuente, D. et al. Corrosion mechanisms of mild steel in chloride-rich atmospheres. *Mater. Corros.* **67**, 227–238 (2016).
23. Zhang, S. et al. Investigating the influence mechanism of hydrogen partial pressure on fracture toughness and fatigue life by in-situ hydrogen permeation. *Int. J. Hydrog. Energ.* **46**, 20621–20629 (2021).
24. Newman, J. C. & Raju, I. S. An empirical stress-intensity factor equation for the surface crack. *Eng. Fract. Mech.* **15**, 185–192 (1981).
25. Liu, Z. G. et al. Corrosion behaviour of low-alloy martensite steel exposed to vapour-saturated CO$_2$ and CO$_2$-saturated brine conditions. *Electrochim. Acta* **213**, 842–855 (2016).
26. Yamashita, M., Miyuki, H., Matsuda, Y., Nagano, H. & Misawa, T. The long-term growth of the protective rust layer formed on weathering steel by atmospheric corrosion during a quarter of a century. *Corros. Sci.* **36**, 283–299 (1994).
27. Asami, K. & Kikuchi, M. In-depth distribution of rusts on a plain carbon steel and weathering steels exposed to coastal-industrial atmosphere for 17 years. *Corros. Sci.* **45**, 2671–2688 (2003).
28. Stahl, K. et al. On the akaganeite crystal structure, phase transformations and possible role in post-excavational corrosion of iron artifacts. *Corros. Sci.* **45**, 2563–2575 (2003).
29. Alcantara, J. et al. An attempt to classify the morphologies presented by different rust phases formed during the exposure of carbon steel to marine atmospheres. *Mater. Charact.* **118**, 65–78 (2016).
30. Refait, P. et al. Electrochemical formation of green rusts in deaerated seawater-like solutions. *Electrochim. Acta* **56**, 6481–6488 (2011).
31. Pineau, S. et al. Formation of the Fe(II–III) hydroxysulphate green rust during marine corrosion of steel associated to molecular detection of dissimilatory sulphite-reductase. *Corros. Sci.* **50**, 1099–1111 (2008).
32. Rammelt, U. & Reinhard, G. The influence of surface-roughness on the impedance data for iron electrodes in acid-solutions. *Corros. Sci.* **27**, 373–382 (1987).
33. Armstrong, R. D. & Burnham, R. A. Effect of roughness on impedance of interface between a solid electrolyte and a blocking electrode. *J. Electroanal. Chem.* **72**, 257–266 (1976).
34. Takahashi, K. Application of cole-cole plot to study of adsorption kinetics at mercury/electrolyte-solution interface. *Electrochim. Acta* **13**, 1609–+ (1968).
35. Tian, H. Y. et al. Corrosion evolution and stress corrosion cracking behavior of a low carbon bainite steel in the marine environments: effect of the marine zones. *Corros. Sci.* **206**, 110490 (2022).
36. Xu, Y. et al. Evaluation of hydrogen permeation into high-strength steel during corrosion in different marine corrosion zones. *Appl. Sci. Basel.* **12**, 2785 (2022).
37. Hardie, D., Charles, E. A. & Lopez, A. H. Hydrogen embrittlement of high strength pipeline steels. *Corros. Sci.* **48**, 4378–4385 (2006).
38. Neeraj, T., Srinivasan, R. & Li, J. Hydrogen embrittlement of ferritic steels: observations on deformation microstructure, nanoscale dimples and failure by nanovoiding. *Acta Mater.* **60**, 5160–5171 (2012).
39. Venezuela, J., Liu, Q. L., Zhang, M. X., Zhou, Q. J. & Atrens, A. The influence of hydrogen on the mechanical and fracture properties of some martensitic advanced high strength steels studied using the linearly increasing stress test. *Corros. Sci.* **99**, 98–117 (2015).
40. Nanninga, N. E. et al. Comparison of hydrogen embrittlement in three pipeline steels in high pressure gaseous hydrogen environments. *Corros. Sci.* **59**, 1–9 (2012).
41. Chatzidouros, E. V., Papazoglou, V. J., Tsiourva, T. E. & Pantelis, D. I. Hydrogen effect on fracture toughness of pipeline steel welds, with in situ hydrogen charging. *Int. J. Hydrog. Energy* **36**, 12626–12643 (2011).
42. Hall, E. O. *Yield Point Phenomena in Metals and Alloys* (Plenum Press, New York, 1970).
43. Chen, Y. Y. et al. Corrosion resistance and mechanical properties of low-alloy steels under atmospheric conditions. *Corros. Sci.* **47**, 1001–1021 (2005).
44. Ma, Y. T., Li, Y. & Wang, F. H. Corrosion of low carbon steel in atmospheric environments of different chloride content. *Corros. Sci.* **51**, 997–1006 (2009).
45. Evans, U. R. Electrochemical mechanism of atmospheric rusting. *Nature* **206**, 980–& (1965).
46. Singh, D. D. N., Yadav, S. & Saha, J. K. Role of climatic conditions on corrosion characteristics of structural steels. *Corros. Sci.* **50**, 93–110 (2008).

47. Melchers, R. E. Effect on marine immersion corrosion of carbon content of low alloy steels. *Corros. Sci.* **45**, 2609–2625 (2003).

48. Stratmann, M. The investigation of the corrosion properties of metals, covered with adsorbed electrolyte layers-a new experimental-technique. *Corros. Sci.* **27**, 869–872 (1987).

49. Stratmann, M. & Streckel, H. On the atmospheric corrosion of metals which are covered with thin electrolyte layers – 1. Verification of the experimental-technique. *Corros. Sci.* **30**, 681–696 (1990).

50. Evans, U. R. & Taylor, C. A. J. Mechanism of atmospheric rusting. *Corros. Sci.* **12**, 227–& (1972).

51. Stratmann, M., Bohnenkamp, K. & Engell, H. J. An electrochemical study of phase-transitions in rust layers. *Corros. Sci.* **23**, 969–985 (1983).

52. Stratmann, M. & Hoffmann, K. Insitu mossbauer spectroscopic study of reactions within rust layers. *Corros. Sci.* **29**, 1329–1352 (1989).

53. Xu, Y., Huang, Y. L., Cai, F. F., Lu, D. Z. & Wang, X. T. Study on corrosion behavior and mechanism of AISI 4135 steel in marine environments based on field exposure experiment. *Sci. Total. Environ.* **830**, 154864 (2022).

54. Kamimura, T., Hara, S., Miyuki, H., Yamashita, M. & Uchidam, H. Composition and protective ability of rust layer formed on weathering steel exposed to various environments. *Corros. Sci.* **48**, 2799–2812 (2006).

55. Yu, J. X. et al. Corrosion behavior of X65 pipeline steel: comparison of wet–Dry cycle and full immersion. *Corros. Sci.* **133**, 276–287 (2018).

56. Li, D. M., Gangloff, R. P. & Scully, J. R. Hydrogen trap states in ultrahigh-strength AERMET 100 steel. *Metall. Mater. Trans. A* **35A**, 849–864 (2004).

57. Zhang, L., Du, M. & Li, Y. Effects of applied potentials on the hydrogen-induced cracking of pipeline steel in low-temperature and low-dissolved-oxygen sea-water. *Corrosion* **68**, 713–719 (2012).

58. Xiong, X. L., Zhou, Q. J., Li, J. X., Volinsky, A. A. & Su, Y. J. Cathodic over-potential and hydrogen partial pressure coupling in hydrogen evolution reaction of marine steel under hydrostatic pressure. *Electrochim. Acta* **247**, 1019–1029 (2017).

59. Zheng, G., Popov, B. N. & White, R. E. Hydrogen-atom direct-entry mechanism into metal membranes. *J. Electrochem. Soc.* **142**, 154–156 (1995).

60. Venezuela, J., Zhou, Q. J., Liu, Q. L., Zhang, M. X. & Atrens, A. Influence of hydrogen on the mechanical and fracture properties of some martensitic advanced high strength steels in simulated service conditions. *Corros. Sci.* **111**, 602–624 (2016).

61. Robinson, M. J. & Kilgallon, P. J. Hydrogen embrittlement of cathodically protected high-strength, low-alloy steels exposed to sulfate-reducing bacteria. *Corrosion* **50**, 626–635 (1994).

62. Newman, J. F. & Shreir, L. L. Role of hydrides in hydrogen entry into steel from solutions containing promoters. *Corros. Sci.* **9**, 631–& (1969).

63. Wang, D. et al. The effect of sulfate-reducing bacteria on hydrogen permeation of X80 steel under cathodic protection potential. *Int. J. Hydrog. Energ.* **42**, 27206–27213 (2017).

64. Sangeetha, R., Kumar, R., Doble, M. & Venkatesan, R. Barnacle cement: an etchant for stainless steel 316L? *Colloid Surf. B* **79**, 524–530 (2010).

65. Lynch, S. Hydrogen embrittlement phenomena and mechanisms. *Corros. Rev.* **30**, 105–123 (2012).

66. Dieter, G. E. *Mechanical Metallurgy* 3rd edn (Mc-Graw Hill, London, 1986).

67. Barnoush, A. & Vehoff, H. Electrochemical nanoindentation: a new approach to probe hydrogen/deformation interaction. *Scr. Mater.* **55**, 195–198 (2006).

68. Devanathan, M. A. V. & Stachurski, Z. Adsorption and diffusion of electrolytic hydrogein in palladium. *R. Soc. Lond.* **270**, 90 (1962).

AUTHOR CONTRIBUTIONS

Y.X.: investigation, methodology, and writing—original draft. Y.H.: supervision, writing—review and editing, and funding acquisition. D.L.: conceptualisation, formal analysis, and supervision. F.C.: data collection and investigation. Z.W.: software and validation. X.W.: formal analysis and supervision. All authors discussed the results and contributed to the final version of the manuscript.

COMPETING INTERESTS

The authors declare no competing interests.

ADDITIONAL INFORMATION

Supplementary information The online version contains supplementary material available at https://doi.org/10.1038/s41529-022-00309-2.

Correspondence and requests for materials should be addressed to Yanliang Huang or Dongzhu Lu.

Reprints and permission information is available at http://www.nature.com/reprints

Publisher's note Springer Nature remains neutral with regard to jurisdictional claims in published maps and institutional affiliations.